

---

Masters Theses

Student Theses and Dissertations

---

Spring 2018

## Controlling phase fractions of 304L-SS in selective laser melting using cooling rate

Eberechukwu Anthony Okoro

Follow this and additional works at: [https://scholarsmine.mst.edu/masters\\_theses](https://scholarsmine.mst.edu/masters_theses)



Part of the [Mechanical Engineering Commons](#)

Department:

---

### Recommended Citation

Okoro, Eberechukwu Anthony, "Controlling phase fractions of 304L-SS in selective laser melting using cooling rate" (2018). *Masters Theses*. 7775.

[https://scholarsmine.mst.edu/masters\\_theses/7775](https://scholarsmine.mst.edu/masters_theses/7775)

This thesis is brought to you by Scholars' Mine, a service of the Missouri S&T Library and Learning Resources. This work is protected by U. S. Copyright Law. Unauthorized use including reproduction for redistribution requires the permission of the copyright holder. For more information, please contact [scholarsmine@mst.edu](mailto:scholarsmine@mst.edu).

CONTROLLING PHASE FRACTIONS OF 304L-SS IN SELECTIVE LASER MELTING  
USING COOLING RATE

by

EBERECHUKWU ANTHONY OKORO

A THESIS

Presented to the Faculty of the Graduate School of the  
MISSOURI UNIVERSITY OF SCIENCE AND TECHNOLOGY

In Partial Fulfilment of the Requirements for the Degree

MASTER OF SCIENCE IN MECHANICAL ENGINEERING

2018

Approved by

Dr. Edward C. Kinzel, Advisor

Dr. Frank Liou

Dr. K. Chandrashekhara

© 2018

Eberechukwu Anthony Okoro

All Rights Reserved

## ABSTRACT

This study examines the thermal profile and the ferrite-austenite phase fractions upon heating and cooling of 304- stainless steel powder via Selective Laser Melting (SLM). Experiments were performed to validate the ABAQUS finite element model, while the phase transformation simulation was performed using MatCalc and ThermoCalc. A correlation between the thermo-mechanical changes in ABAQUS and the microstructural changes from MatCalc was obtained by matching their cooling rates. The result indicates that cooling rate has a significant effect on the phase fractions of FCC and BCC formed in 304L stainless steel via the SLM process. The results also indicate that for high cooling rates (typically  $> 10^5$  K/s and consistent with laser powers  $\geq 100$ W) the proportions of FCC and BCC were comparable, with FCC phase about 55% and BCC about 45% of the solidified matrix. This result was similar to the results predicted by the Scheil Gulliver model suggesting high cooling rates follow a diffusionless transformation process.

For lower cooling rates, the fractions of FCC increased and that of BCC decreased progressively such that the phase fraction of FCC was greater than 91% with a cooling rate of 3400K/s which corresponds to a laser power of 40W. Such relatively low cooling rate around the phase transformation temperature (i.e. 900K to 450K) is an indication of possible diffusional transformation where the BCC ( $\delta$ ) phases transform to an FCC ( $\gamma$ ) phase.

A higher FCC grade stainless steel has better corrosion properties and produces less magnetic interference in certain critical applications and was another motivation for this study in addition to establishing a process of altering the phase fractions of metals by a cooling-rate only control in SLM.

## ACKNOWLEDGMENTS

I would like to express my sincere gratitude to my thesis advisor, Dr. Edward Kinzel, Department of Mechanical & Aerospace Engineering, Missouri University of Science and Technology, Rolla, for his patience and understanding through this research experience. I appreciate his vast knowledge in various subjects and for his guidance throughout the research while allowing me to be creative and take ownership of my work.

I also want to thank Dr. Frank Liou and Dr. K. Chandrashekhara of Mechanical & Aerospace Engineering Department, Missouri S&T for agreeing to serve on my thesis committee. I must also acknowledge Qizi Zhang for providing initial guidance in developing the heat flux subroutine for the ABAQUS model, and Cody Lough for providing experimental data to validate results from the ABAQUS simulation.

Finally, I owe many thanks to my wife and best friend, Mobilia, for her understanding, encouragement, editing assistance and support over the many months of working persistently on this research, as well as my son, Chikwado, with whom I was inspired to complete this work.

## TABLE OF CONTENTS

	Page
ABSTRACT .....	iii
ACKNOWLEDGMENTS .....	iv
LIST OF ILLUSTRATIONS .....	vii
LIST OF TABLES .....	x
 SECTION	
1. INTRODUCTION.....	1
1.1. SLM OVERVIEW .....	2
1.2. MOTIVATION .....	4
1.3. OBJECTIVE .....	4
2. LITERATURE REVIEW .....	6
3. PHASE TRANSFORMATION MODELING .....	11
3.1. OVERVIEW OF PHASE TRANSFORMATION.....	12
3.1.1. Scheil Model (Diffusionless Transformation) .....	12
3.1.2. Kinetic Transformation (Diffusional) Model .....	14
3.2. PHASE TRANSFORMATION MODEL ANALYSIS .....	18
3.2.1. Austenite ↔ Ferrite Transformation .....	19
3.2.2. Results from MatCalc .....	22
4. FINITE ELEMENT ANALYSIS .....	32
4.1. ABAQUS MODEL SIMULATION .....	33
4.2. GENERAL PROCESS SETUP .....	34
4.3. PROCESS MODEL .....	36
4.3.1. Temperature-Dependent Thermal Conductivity .....	36

4.3.2. Density .....	41
4.3.3. Temperature Dependent Specific Heat .....	41
4.4. HEAT FLUX DISTRIBUTION.....	42
4.4.1. Metallographic Images.....	43
4.4.2. ABAQUS Output Graphic .....	50
4.4.3. Cooling Rate.....	58
5. RESULTS AND DISCUSSIONS .....	66
6. CONCLUSION .....	69
APPENDICES	
A. COOLING RATE TABLES .....	71
B. FORTRAN CODES .....	74
BIBLIOGRAPHY .....	78
VITA... ..	82

## LIST OF ILLUSTRATIONS

Figure	Page
3.1. Schematic Representation of the Scheil–Gulliver Model.....	12
3.2. Interstitial Diffusion by Random Jumps in a Concentration Gradient .....	15
3.3. Schaffler DeLong (FN) Diagram for Stainless Steel Weld Metal.....	19
3.4. Phase Fractions Present in Fe-Cr-Ni for the Cooling Rate 5000C/s .....	23
3.5. Cooling Rate Curve and FCC Phase Fraction-Time Curve at 5000C/s for 304L-SS.....	24
3.6. Phase Fractions Present in Fe-Cr-Ni for the Cooling Rate 10000C/s .....	24
3.7. Cooling Curve and FCC Phase Fraction-Time Curve at 10000C/s for 304L-SS .....	24
3.8. Phase Fractions Present in Fe-Cr-Ni for the Cooling Rate 25000C/s .....	25
3.9. Cooling Curve and FCC Phase Fraction-Time Curve at 25000C/s for 304L-SS .....	25
3.10. Phase Fractions Present in Fe-Cr-Ni for the Cooling Rate 50000C/s .....	25
3.11. Cooling Curve and FCC Phase Fraction-Time Curve at 50000C/s for 304L-SS .....	26
3.12. Phase Fractions Present in Fe-Cr-Ni For the Cooling Rate 100000C/s .....	26
3.13. Cooling Curve and FCC Phase Fraction-Time Curve at 100000C/s for 304L-SS .....	26
3.14. Phase Fractions Present in Fe-Cr-Ni for the Cooling Rate 200000C/s .....	27
3.15. Cooling Curve and FCC Phase Fraction-Time Curve at 200000C/s for 304L-SS .....	27
3.16. Phase Fractions Present in Fe-Cr-Ni For the Cooling Rate 500000C/s .....	27
3.17. Cooling Curve and FCC Phase Fraction-Time Curve at 500000C/s for 304L-SS .....	28
3.18. Phase Fractions Present in Fe-Cr-Ni for the Cooling Rate 1000000C/s .....	28
3.19. Cooling Curve and FCC Phase Fraction-Time Curve at 1000000C/s for 304L-SS .....	28
3.20. Cooling Rates for FCC vs BCC Phase Fractions on Fe-Cr-Ni Alloy in 304L-SS .....	30
3.21. Generic Phase Diagram of Fe-Cr-Ni (304L-SS) Showing Possible Phases and their Corresponding Temperature Ranges.....	30



4.1. Schematic of SLM Process Setup [44] .....	34
4.2. Temperature-Dependent Thermal Conductivity Plot for 304L Stainless Steel .....	40
4.3. Temperature-Dependent Conductivity Plot for Argon .....	40
4.4. Temperature Dependent – Specific Heat Plot for 304L Stainless Steel .....	42
4.5. Line Scan on Last Layer with Laser Power 200W and Point Distance 60 $\mu\text{m}$ .....	44
4.6. Top Layers of Structure Built with Laser Power 100W and Point Distance 60 $\mu\text{m}$ .....	44
4.7. Top Layers of Structure Built with Laser Power 150W and Point Distance 60 $\mu\text{m}$ .....	45
4.8. Top Layers of Structure Built with Laser Power 200W and Point Distance 60 $\mu\text{m}$ .....	45
4.9. Experimental Melt Pool Width.....	46
4.10. Experimental Melt Pool Depth.....	46
4.11. An Ellipse with Focal Points Indicated by the Black Dots.....	48
4.12. Melt Pool Width for 200W Laser Power (248 $\mu\text{m}$ ).....	50
4.13. Melt Pool Depth for 200W Laser Power (231.1 $\mu\text{m}$ ).....	51
4.14. Melt Pool Width for 150W Laser Power (213 $\mu\text{m}$ ).....	51
4.15. Melt Pool Depth for 150W Laser Power (137.6 $\mu\text{m}$ ).....	52
4.16. Melt Pool Width for 100W Laser Power (159.7 $\mu\text{m}$ ).....	52
4.17. Melt Pool Depth for 100W Laser Power (115.9 $\mu\text{m}$ ).....	53
4.18. Melt Pool Width: Experimental and Simulated Curves for 40 $\mu\text{m}$ Point Distance .....	54
4.19. Melt Pool Depth: Experimental and Simulated Curves for 40 $\mu\text{m}$ Point Distance .....	55
4.20. ABAQUS Output Graphic Highlighting Paths, XY-Data and Query .....	59
4.21. ABAQUS Output Graphic Highlighting Time-frame and Selected Path Nodes.....	60
4.22. Example of an XY-Data Graph from ABAQUS .....	60
4.23. Cooling Curve for 200W Laser Power .....	61
4.24. Cooling Curve at Constant Slope from Fig. 4.23 .....	61

4.25. Cooling Curve for 150W Laser Power .....	62
4.26. Cooling Curve at Constant Slope from Fig. 4.25 .....	62
4.27. Cooling Curve for 100W Laser Power .....	63
4.28. Cooling Curve at Constant Slope from Fig. 4.27 .....	63
4.29. Cooling Curve for 50W Laser Power .....	64
4.30. Cooling Curve at Constant Slope from Fig. 4.29 .....	64
4.31. Cooling Curve for 40W Laser Power .....	65
4.32. Cooling Curve at Constant Slope from Fig. 4.31 .....	65
5.1. Scheil Model Showing FCC-Phase Fraction for Fe (70%), Cr (18%) and Ni (12%) in 304L-SS (ThermoCalc).....	67
5.2. Scheil Model Showing BCC-Phase Fraction for Fe (70%), Cr (18%) and Ni (12%) in 304L-SS (ThermoCalc).....	67

## LIST OF TABLES

Table	Page
3.1. Material Properties of 304L-Stainless Steel .....	21
3.2. Phase Fractions of FCC in Fe-Cr-Ni for Different Cooling Rates via MatCalc.....	29
4.1. Experimental Melt Pool Width for a 40 $\mu$ m Point Distance .....	47
4.2. Experimental Melt Pool Depth for a 40 $\mu$ m Point Distance.....	47
4.3. Mn for Different Laser Powers.....	48
4.4. a and b for Different Laser Powers.....	49
4.5. Melt Pool Width for a 40 $\mu$ m Point Distance .....	53
4.6. Melt Pool Depth for a 40 $\mu$ m Point Distance .....	54
4.7. c and M <sub>j</sub> for a 40 $\mu$ m Point Distance.....	56
4.8. Correction Factors for Heat Penetration and Heat Flux .....	57
4.9. a and b for a 40 $\mu$ m Point Distance .....	57

## 1. INTRODUCTION

During SLM process, rapid melting and solidification of powder particles occurs which produces a very large temperature gradient and determines to a large extent the nature of the resulting microstructure. The mechanisms for most melting and solidification process with respect to the microstructural evolutions can be described either by kinetic and/or thermodynamic models. The kinetic model describes the diffusion controlled process such as grain growth, nucleation and recrystallization, while the thermodynamic models describes the phases present during melting or solidifications given certain conditions using the principle of equilibrium defined by the Gibbs free energy.

A 304L-stainless (Austenitic) steel powder was used for this study. The stable phases present in austenitic stainless steels are austenite (FCC-face centered cubic structure) and ferrite (BCC-body centered cubic structure) or a combination of FCC and BCC. There's also a possibility for martensite to precipitate at room temperature. However, the driving force for its formation maybe insufficient for it to form spontaneously, so it typically is not considered for rapid laser melting and solidification.

In order to simulate the heating, melting and solidification process, an ABAQUS model was developed consisting of a powder bed evenly spread unto a substrate. A single laser pulse of very high intensity is applied to selected points on the powder bed so that rapid melting and solidification occurs. When the laser beam completes a scan through the powder bed, a new powder layer is deposited unto the bed and the process continues until the part is built.

## 1.1. SLM OVERVIEW

Selective Laser Melting is a type of Additive Manufacturing technique that is gaining a lot of attention in recent times (late 1980's till date [1]) due its ability to manufacture high quality components of complex shapes and properties. Unlike EDM (Electron Beam Melting) it can produce a wider range of metallic components using a laser beam rather than electron beam which is only suitable for a limited number of metal powders. The major challenge using SLM is that the high temperature gradients that occur during SLM can also lead to residual stresses inside the final part which can compromise its mechanical properties.

Typically, SLM involves heating and melting over the surface of successive layers of powder using a laser beam guided by a CAD program. Upon irradiation, the powder particles gain sufficient thermal energy and melts forming a melt pool at the point of irradiation. As the laser moves ahead, the molten pool cools down and solidifies. Melting of the powder during SLM allows fully dense materials to be produced directly in contrast to DMLS (Direct Metal Laser Sintering) which requires post-processing, infiltration, sintering, and hot isostatic pressing to achieve fully dense parts (Kruth et al.). It is therefore of extreme importance to ensure the powder scanning zone is fully melted during the SLM process.

Two common scan methods utilized to melt the powder are: (i) Pulsed Laser Scan and (ii) Moving Laser Scan. Just as the name implies, in the pulsed laser scan method, the laser is stationed at predetermined position on the powder bed over a specific period of time (usually in microseconds), then relocates to the next position on the powder bed and this process continues until the scan is complete. In the moving laser scan, the laser is in a continuous motion along a predetermined scan path and melts the powder as it moves along. After a complete scan is made, the build platform is lowered and a new layer of powder is deposited unto the build platform so that the process is repeated until the part is fully built. The non-irradiated material remains in the building cylinder and is used as a support structure

for subsequent layers. After the end of the process, the unused powder is sieved and can be reused [2].

The physics of the SLM process is quite complex and requires a combination of time dependent thermo-mechanical correlations to accurately predict the structural and microstructural changes associated with this process. To a great degree this depends on the effective thermal conductivity of the powder material so that the equations of heat transfer is coupled together with equations of powder consolidation kinetics [3]. Some 3D models have been proposed to account for the various changes encountered during the SLM process and usually consists of the balance of thermal energy and the associated boundary conditions.

SLM finds particular application in aerospace, automotive, biomedical technology, energy and tool manufacturing. Kruth et al. [4] published a biocompatible metal framework for dental prostheses and Wehmoller et al. [5] reported body implants of cortical bone, mandibular canal segment, and support structures or tubular bone made from 316L stainless steel. Smurov's research group demonstrated a mini pump die and small parts with conformal cooling channels,[6] displaying the ability of SLM to create small and complex parts with Inox 904L steel. The research contributed to the fabrication of the diverter thimbles in the cooling system of the International Thermonuclear Experimental Reactor (ITER) [7]. In a similar manner, Garcia et al. [8] incorporated spiral conformal cooling channels for injection molding and found that both cycle time and part quality were dramatically improved. The first paper on SLM of steel light-weight structures was reported by Santorinaios et al.[9] on the crush behavior of such structures. Following this, there have been more research works that investigated the quasi-static and blast response, compressive properties, shock response and failure mechanism of the steel lattice structures.

## 1.2. MOTIVATION

Selective laser melting process is a complex process involving both time and temperature dependent changes. These changes depend largely on several variables relating to the material properties and input parameters. The material properties include conductivity, specific heat, porosity, powder grain size, density, emissivity and absorptivity; while the input parameters include laser power, pulse duration, point distance, laser beam diameter and scan strategy. Several models have been developed to study the thermal evolutions during this process. However, there are little or no study relating how the microstructure of the material evolves with the changes in the thermal profile in time when the input parameters are varied. A correlation of this nature provides a means of analyzing the effects of different input parameters on the temperature distribution and microstructure as the material is heated up and cooled down, thus saving costs and time wasted in several repetitive experiments and providing a means of altering the microstructure by controlling the input parameters. This study shows how such a correlation can be achieved using 304L-Stainless Steel as a case study. The microstructural transformations were limited only to phase fractions to keep the study as basic as possible. A graph relating the changes in phase fractions and temperature profile in time was developed, while the temperature distribution was described by a unique subroutine.

## 1.3. OBJECTIVE

This research examines how the FCC (austenite) phase can be increased from a partially austenitic stainless steel which is typical for the matrix obtained from the SLM process; to a fully austenitic 304L-SS ( $> 90\%$  FCC and  $< 1\%$  BCC) by controlling the cooling rates only. Therefore, this study also draws a correlation between the cooling rates and the phase fractions of FCC and BCC formed during and after consolidation of the molten

powder. Most studies on fully austenitic stainless-steel uses high amounts of Ni > 20% to obtain a fully austenitic alloy. For example, Kujanpaa et al [15] used Ni of 25%; T. Ogawa et al [16] used Ni of 20% Backman et al. [17] used Ni of 22% to obtain a fully austenitic stainless steel. The % composition of Ni for the 304L-SS sample powder in this study was 12% which is typical for standard 304L-SS; so that the increase in FCC achieved can only be attributed to changes in the cooling rates.

In addition, ferrite has detrimental effects on the corrosion resistance of weldments or the solidified part if that part is going to be subject to harsh corrosion environments [18], [19]. There are also applications where magnetic properties of the ferrite can interfere with the performance of the end product [20] (austenite is non-magnetic). Although this research focuses only on 304L-SS, the ideas and methodology adopted here can be applied to other alloys as well.



## 2. LITERATURE REVIEW

As systems and designs become more and more complex with the recent advancement in technology, new materials and very intricate parts need to be developed to meet with growing demands for productivity, reliability, precision measurement and increased efficiency. Traditional methods of producing components by casting and forging are limited not only by the component geometric properties and material composition, but also by the surface finish, residual stresses and defects requiring post-heat treatment and machining, can be labor intensive and requires great human skill and dexterity, high tooling costs and long set times. [21]

The development of additive manufacturing has proven to take the science of manufacturing to greater frontiers by enabling the manufacture of very intricate parts that were once only wishful thinking. Although additive manufacturing offers greater benefits especially in the manufacture of specialized intricate higher quality parts it also has its own setbacks. It is limited to only small production quantity and dimensions due to the size of the equipment. Example, turbine blades are primarily precision cast by additive manufacturing to a complex geometry and microstructure constraints (i.e. single crystalline, polycrystalline, directionally solidified) whereas forgings is more suitable for turbine disks and casings subjected to dynamic loads. [22]

Components made from SLM may also see more oxidation than conventional casting process [23]. Further the lack of in site process control or validation of material microstructure and mechanical properties limit additive manufacturing to mostly non-structural applications [24]. William Frazier [25] noted specific challenges that needed to be addresses with AM technologies such as: i) developing in-process sensing, monitoring and controls; ii) controlling machine to machine variability (iii) alternatives to conventional

qualification methods (iv) development of integrated structural and material design tools (v) developing physical models relating microstructure, properties and performance (vi) improving surface roughness of formed parts and better material fatigue control.

Standardization is another major step in progress to help expedite the advancement of AM processes. In 2013 ISO/TC 261 Additive Manufacturing made two standards; ISO/ASTM 52915 (standard specification for additive manufacturing file format) and ISO/ASTM 52921 (standard terminology for additive manufacturing coordinate systems and test methodologies). Other standards in the making include ISO/CD 17296-1 (rapid prototyping terminologies); ISO/CD 17296-3 (rapid prototyping test methods), ISO/CD 17296-4 (rapid prototyping data processing). In 2013, NIST awarded two grants: (i) \$5 million to create a certification standard to be used in the production of high-value 3D printed designs; and (ii) \$2.4 million to develop tools to analyze the quality of 3D printed parts [26].

Despite the setbacks, additive manufacturing has a bright future in the manufacturing industry and its usage will see increasing trends as more economic ways of producing large scale quantities of parts becomes available with improvements in current technology. Some notable benefits of additive manufacturing include (i) efficiency in material usage by building parts layer-by-layer; (ii) no fixtures, tools or coolant required; (iii) intricate parts can be produced since there is no tooling constraints involved; and (iv) very economical for small batch production and does not require costly set-ups [27]. Additive manufacturing comes in different types and can be classified into six categories;

1. Vat photopolymerization
2. Powder bed fusion
3. Metal extrusion
4. Material jetting

5. Binder jetting
6. Direct energy deposition

The focus of this paper however is only on the Selective Laser Melting process which is under the powder bed fusion category. The process of SLM is already discussed in the introductory section. SLM differs from most other AM processes in that the powder is not merely fused together but actually melted into a single layer homogeneous part, producing components with fewer voids than most other AM methods. Since materials will fully melt during the SLM process, one would equally expect a change in the microstructure as a result of melting and cooling of the melt pool. In fact, that is essentially the case. This resulting change in microstructure and the ability to control this change has attracted a lot of research interest. Lore Thijs et al studied the effect of the scanning parameters and scanning strategy on the microstructure of ti-6AL-4v and found that the direction of the elongated grains is directly related to the process parameters [28].

E. Yasa et al. [29] investigated the effect of re-melting on the surface roughness of the solidified part. It was shown that the pores formed in between neighboring melt pools disappear with laser re-melting after every layer is applied, leading to a higher density part with improved mechanical properties. It was also observed that SLM also refined the microstructure. Wei Chin et al. [30] used electromagnetic flux density in SLM; although the full mechanism is still unclear, this method shows good application to produce microstructure controllable bioimplant products with complex shapes and other non-magnetic alloys like metallic glass using additive manufacturing. Susan Dadbakhsh and Liang Hao [31] studied the influence of powder bed thickness on the microstructural features such as granular, coralline-like and particulate appearance depending on the layer thickness, laser power and scanning speed. From their research, the highest comparative micro hardness was formed

using a smaller layer thickness, high laser power and low scanning speed with well bonded and uniform distribution of fine and stable particles of Al matrix.

This study concentrates on the study of the effects of cooling rate on the microstructure of 304L- stainless steel with greater emphasis in manipulating the cooling rate to alter the microstructure of 304L stainless steel from an austenite plus ferrite matrix to a fully austenitic matrix. 304L-SS is only used here as a case study to show the correlation between cooling rates and the microstructural changes that a material undergoes during cooling. To ensure that the changes in the microstructure can be attributed to the cooling rate, all other parameters are held constant while only the power source is manipulated. It will also be seen subsequently in this study that the cooling rate evolves with time over the entire cooling duration irrespective of the magnitude of the laser power used; and is by no means a fixed parameter over the entire cooling process.

This study takes a back-step approach in predicting the microstructure of 304L-SS in the consolidated metal. 304L-SS powder conventionally contains fractions of ferrite, typically between 8 to 20% ferrite, with the remaining fractions mostly comprising austenite [32]. Using simulation tools, (MatCalc and ThermoCalc) various cooling rates are simulated and the phase fractions recorded. This study seeks to transform 304L-SS powder from a partial austenite matrix to a fully austenitic alloy (> 90%). Next the SLM process is modeled and simulated with ABAQUS using different laser powers. The cooling rates extracted from ABAQUS are then compared to the initial MatCalc simulation for correspondence. Cooling rates from MatCalc matching the cooling rates from the ABAQUS model are then mapped so that a correlation between the cooling rates and phase fractions of FCC and BCC can be obtained for a given power input.

An experiment was performed to validate the correctness of the ABAQUS model by comparing the width and depth of the melt pool via ABAQUS to the width and depth of the

solidified melt via experiment. Due to the fact that cooling in SLM is quite rapid (microseconds) it is very difficult to measure in-process cooling rates. Therefore, the assumption adopted in this study is that dimensions of the solidified melt pool via experiment corresponding with the dimensions obtained from the ABAQUS simulation given the same conditions, has identical thermal profiles and corresponding cooling rates.

ABAQUS (a finite element simulation tool) and MatCalc (a thermodynamic and kinetic transformation simulation tool) are two different independent simulation tools. This strategy combines the capability of ABAQUS in predicting the thermo-mechanical changes and MatCalc in predicting the microstructural transformations into one robust approach that effectively correlates their thermo-mechanical and microstructural outcomes.

### 3. PHASE TRANSFORMATION MODELING

As the laser hit the surface of the powder bed, the metal powder absorbs radiant energy from the beam, reflects some energy, conducts some energy to neighboring powder particles, while some energy is lost in the space between particles and others through convection and evaporation in the melt pool. Of course, as the powder bed is irradiated and gains heat energy from the laser beam, its temperature increases accordingly. If the intensity of the laser beam and time of exposure is sufficient enough, this increase in the powder bed temperature reaches solidus (i.e. 1697K for 304L-SS) above which the powders begin to melt into liquid metal. This transition point between solid powder-to-liquid metal is very critical to a more realistic model of the heat transfer process due to latent heat. The powder is fully melted into a liquid pool at the liquidus temperature (i.e. 1727K for 304L-SS). Conversely when the laser goes out or is stopped (i.e. for a pulsed laser beam) or transitions further away (i.e. for a moving laser beam) the temperature of the molten pool falls below the liquidus and the solidification process begins until a solid structure is formed at room temperature (i.e. 300K for this paper). The next scan begins with a new powder layer and the new solidified layer builds up from bottom to the top until a fully built part is established. In order to capture the different changes occurring during the SLM process; the model is categorized into three stages (i.e. pre-heating, melting and re-solidification) and the changes evolving during the process i.e. conduction, heat flux, absorption, evaporation, latent heat, etc. are discussed and represented on the applicable stages of the model. These changes mentioned above are needed to effectively model the SLM process and ensure the model developed is a fairly accurate representation of the process.

### 3.1. OVERVIEW OF PHASE TRANSFORMATION

The next sub-sections describe the diffusionless and diffusional model. The diffusionless model is basically the Scheil-Gulliver model typical with high cooling rates while the diffusional model depicts the phase transformation at lower cooling rates.

**3.1.1. Scheil Model (Diffusionless Transformation).** The Scheil model describes a diffusionless transformation process. Figure 3.1 illustrates the Scheil diffusionless where  $T$  is the temperature and  $X$  is the concentration of solutes formed during the cooling process.

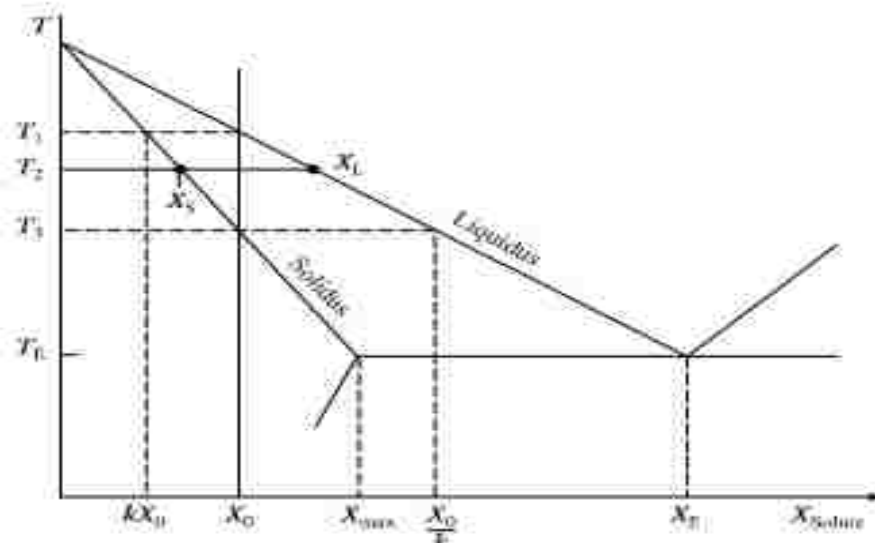


Figure 3.1. Schematic Representation of the Scheil–Gulliver Model (David Porter et al, 2009)

In this process, the first solid that forms contain less of the second component. Assuming no diffusion takes place in the solid state and that the liquid composition is kept homogenous by efficient stirring during solidification and also assuming solidification is unidirectional, Figure 3.1 shows that the first solid forms as the cooled end reaches  $T_1$  with a concentration of  $KX_0$  moles of solid. Since  $KX_0 < X_0$ , the solute will be rejected into the

liquid. This raises the concentration of the liquid above  $X_0$  and reduces the temperature at the solid/liquid interface below  $T_1$  so that further solidification occurs with the next layer of solid slightly richer in solute concentration than the first. At any stage during solidification, local equilibrium can be assumed to exist at the solid/liquid interface so that at any given interface temperature, the compositions of the solid/liquid interface will be described by the equilibrium or thermodynamic phase diagram only. Since no solid diffusion occurs, the separate layers of solid formed retains their original composition until all liquids is transformed to solid.

The amount of the second component in the sample expressed in terms of concentration in the solid is expressed as;

$$\int_0^g C_s dx + (1-g) C_L = C_x \quad (1)$$

where

$C_L$ : concentration of solute at liquidus (i.e. >1723K)

$C_S$ : concentration of solute at solidus (i.e.  $\geq 1697K$  but  $< 1723K$ )

$g$ : fraction solidified

$k$  (partition coefficient) =  $C_S/C_L$

Differentiating Equation (1) with respect to  $g$ ,

$$C_S + (1-g) \frac{dC_L}{dg} - C_L = 0 \quad (2)$$

Replacing  $C_S$  with  $kC_L$  and rearranging Equation (2),

$$\frac{dC_L}{C_L} \left( \frac{1-k}{1-g} \right) dg \quad (3)$$

Integrating Equation (3),

$$C_L = - (1-k) \ln(1-g) + \text{constant}$$

Just before solidification begins,



$$g = 0, C_L = C_\infty$$

$$C_L = C_\infty (1-g)^{k-1} \quad (4)$$

from  $k = C_s/C_L$

$$C_L = C_s/k$$

Substituting into Equation (4)

$$C_s = kC_\infty (1-g)^{k-1} \quad (5)$$

Equation (5) is known as Scheil equation [33].

**3.1.2. Kinetic Transformation (Diffusional) Model.** Unlike the diffusionless or massive transformation, the diffusional transformation is rather very complex process involving both thermodynamic and kinetic mechanisms. This even gets more complicated with multicomponent systems. The goal of this study is not to spend time on discussing the various complex mechanisms, however, a glance at some basic concept with diffusional transformation is mentioned here.

The diffusional transformation here refers to solid-state diffusion only. Diffusion typically occurs at microstructural discontinuities such as grain boundaries, dislocations, vacancies, interstitials, etc. Therefore, the diffusion mechanism will depend on the nature of the available site in the lattice. Typically, substitutional atoms diffuse by a vacancy mechanism while interstitial atoms diffuse interstitially by forcing their way between larger atoms (David Porter et. al. [34]). Figure 3.2 illustrates the mathematical model for interstitial diffusion.

From Figure 3.2a and 3.2b., David et al. (2009), assuming (1) and (2) represents two adjacent atomic planes such that an average interstitial atom jumps  $r_s$  times per second randomly. Statistically there exists equal probability of the atom jumping into any one of the six adjacent sites. If plane (1) contains  $n_1$  B-atoms per  $m^2$ , the number of atoms jumping

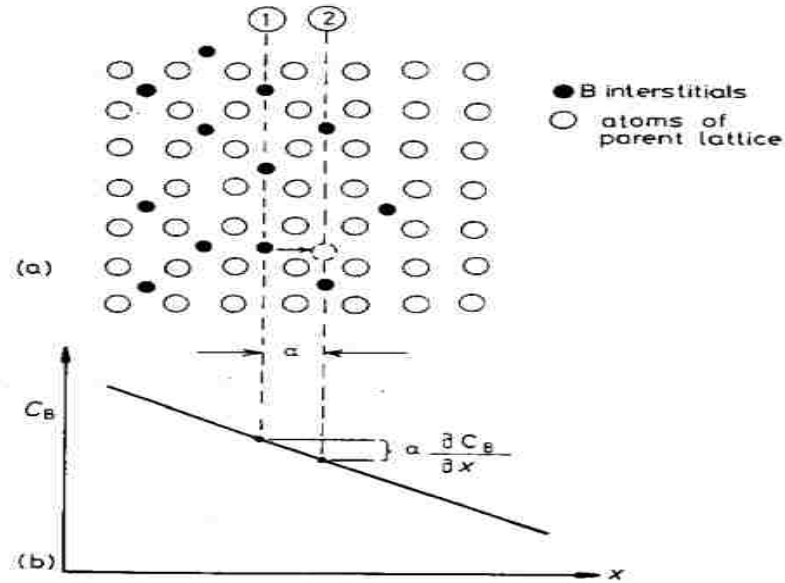


Figure 3.2. Interstitial Diffusion by Random Jumps in a Concentration Gradient (“Phase Transformation in Metals and Alloys”; David Porter et al., 2009)

from plane (1) to (2) in one second is  $J_{B1}$  and can be expressed as;

$$J_{B1} = \frac{1}{6} \Gamma_B n_1 \text{ atoms/m}^2\text{sec}$$

For atoms jumping from plane (2) to plane (1) we can express  $J_B$  as

$$J_{B2} = \frac{1}{6} \Gamma_B n_2 \text{ atoms/m}^2\text{sec}$$

If we assume a net flux of atoms moving from left ( $n_1$ ) to right ( $n_2$ ) then

$$J_{B(\text{net})} = J_{B1} - J_{B2} = \frac{1}{6} \Gamma_B (n_1 - n_2) \quad (6)$$

If the concentration gradient normal to the plane is given as  $dc/dx$ ; then

$$C_1 - C_2 = -\alpha \frac{dC}{dx}$$

where  $\alpha$  is the plane separation;

$$C_1 = \frac{n_1}{\alpha} \text{ and } C_2 = \frac{n_2}{\alpha}$$

hence Equation (6) becomes

$$J_{B(\text{net})} = - \left[ \frac{1}{6} \Gamma_B \alpha^2 \right] \frac{\partial C_B}{\partial x} \quad (7)$$

$D_B$  intrinsic diffusivity or the diffusion coefficient of B ( $\text{m}^2/\text{s}$ ) is the term inside the bracket in Equation (7), i.e.

$$D_B = \frac{1}{6} \Gamma_B \alpha^2 \quad (\text{David Porter et al.}) \quad (8)$$

For a thermally activated migration, the atoms vibrate about their positions of minimum potential energy more violently due to the thermal energy introduced. If an interstitial atom vibrating with a mean frequency  $\nu$  in the x-direction and making  $z$  attempts per second to jump into the next site, then the fraction of these attempts that are successful is given as

$$\exp(-\Delta G_m/RT)$$

and

$$\Gamma_B \text{ (no of jumps per second)} = z\nu \exp - \frac{\Delta G_m}{RT} \quad (9)$$

$G_m$  is the activation energy for the migration of the interstitial atom

Substituting Equation (9) into Equation (8)

$$D_B = \left[ \frac{1}{6} \alpha^2 z\nu \exp \frac{\Delta S_m}{R} \right] \exp \left( - \frac{\Delta H_m}{RT} \right) \quad (\text{David Porter et al; 2009}) \quad (10)$$

where

$z$ : no of sites surrounding the thermally activated atom

$\nu$ : mean frequency of vibration

$\Delta H_m$ : activation enthalpy

$\Delta S_m$ : activation entropy

$R$ : universal gas constant

Most practical transformation however occurs as a non-steady state diffusion where the concentration varies with both  $x$  and time  $t$ . This relationship can be expressed by the Fick's second law of diffusion;

$$\frac{\partial C_B}{\partial t} = \frac{\partial}{\partial x} \left( D_B \frac{\partial C_B}{\partial x} \right) \quad (11)$$

assuming  $D_B$  (diffusion coefficient of B) remains constant throughout the diffusion transformation, Equation (11) can be reduced to

$$\frac{\partial C_B}{\partial t} = D_B \frac{\partial^2 C_B}{\partial x^2} \quad (12)$$

Even with these equations above, the diffusion process can still be seemingly complicated especially for multicomponent systems where one must carefully distinguish between interstitial and substitutional components as well as vacancies to account for other thermodynamically non-equilibrium process approaching equilibrium. Some constitutive equations relating the internal state variable to the kinetic equations can be solved either by the Fick's first and second law, however, some can only be obtained experimentally [35].

From Alope et al. (2017), the thermodynamic extrema principle (TEP) has been quite successful in the effective treatment of non-equilibrium material systems capable of providing diffusion equations for multicomponent systems and the evolution equations for grains in polycrystals or for precipitates embedded in the matrix. The TEP represents an alternative to the classical phenomenological equations approach. TEP was originally formulated by L. Onsager in 1945 but only became an efficient tool in material science in the last two decades with several literatures published about this concept [36].

From Alope et al. (2017), if a discrete thermodynamic parameter is used to characterize a system, the TEP formulated using these discrete parameters can provide evolution equations for the rates of change of these characteristics parameters e.g. radii of

grains, precipitate in grain growth, shape parameters of a precipitate of a given fixed composition etc. Implementation of the TEP is utilized in MatCalc which is the software used in performing the kinetic transformation for this case study. TEP strategies are integrated in the MatCalc software so that this study only focuses on the analysis results obtained via MatCalc.

### **3.2. PHASE TRANSFORMATION MODEL ANALYSIS**

MatCalc 6.0 was used to perform the diffusional and thermodynamic phase transformation simulation while ThermoCalc 2017a was used to perform the diffusionless Scheil model analysis on 304L- Stainless Steel. The thermodynamic method used in MatCalc and ThermoCalc is based on the CALPHAD methods and CALPHAD type database. The CALPHAD method uses experimental data on phase equilibrium in a system at known temperatures and pressures obtained from thermophysical and thermochemical studies to develop realistic mathematical models that represents the phases present at a given temperature under consideration. These mathematical models use various physical phenomenon such as Gibbs free energy, laws of equilibrium, laws of diffusion, crystal interfaces and microstructural migration, physics of nucleation, growth and diffusional transformation with some ancillary parameters to predict various behaviors, states, quantities and phases during phase transformation. These mathematical models get stored in a CALPHAD database and used with sophisticated algorithms to predict phase transformations of various materials composition. Due to the complexity of the algorithms and mathematical models used in MatCalc and ThermoCalc, this study only focuses on using these powerful tools to determine the phase fractions of ferrite and austenite upon consolidation of 304L Stainless Steel from molten state.

**3.2.1. Austenite ↔ Ferrite Transformation.** The mechanisms of microstructural transformation in austenitic stainless steels have been subject to different interpretations. In austenitic stainless steels, a three-phase reaction region ( $L + \delta + \gamma$ ), which can be either eutectic or peritectic, exists for compositions of over 15 wt% Cr and 10 wt% Ni according to the Fe–Cr–Ni ternary phase diagram [37]. Figure 3.3 shows the Schaffler-DeLong diagram for stainless steel weld metal.

The DeLong diagram (Fig. 3.3) is customarily used in predicting the amount of ferrite likely to be present in a weld deposit made from the wrought product. Plotting the composition of the wrought plate or bar product will indicate how much ferrite might be present if the material were re-melted or welded. However, this is not a very reliable indicator of the ferrite content in the annealed product. More accurate ferrite content can be determined through metallographic examination or by using sensitive magnetic instruments (magnetic permeability).

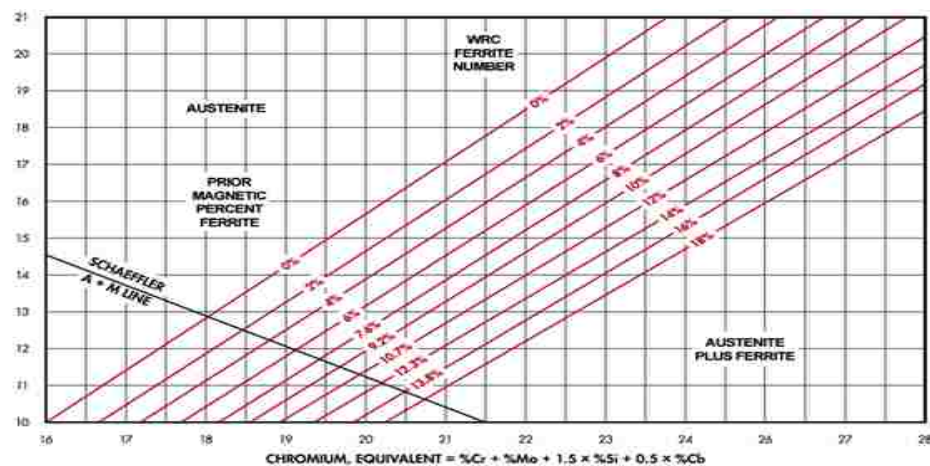
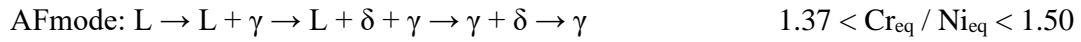
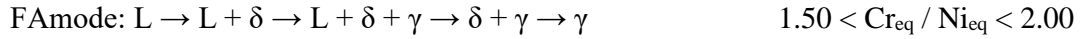


Figure 3.3. Schaffler DeLong (FN) Diagram for Stainless Steel Weld Metal (<http://www.bssa.org.uk/topics.php?article=121>)

Suutala [38] concluded that the solidification sequence of a range of AISI 300 series steels by autogenous gas tungsten arc (GTA) welding was mostly affected by composition while the cooling rate was only of secondary importance. Huang et. al., and Congfeng et. al. [39], [40] suggests that the cooling rates plays a significant role on whether the three-phase region can solidify with primary  $\delta$  ferrite or primary  $\gamma$  phase depending on the % Cr. There exists a view that the  $\delta \rightarrow \gamma$  transformation occurs by a diffusionless massive transformation since with such high cooling rates associated with laser melting, there is not enough time for redistribution of elements upon cooling to room temperature; so that the micro-segregation is complete at the end of the liquid to solid transformation with no further diffusion or migration of elements possible. J.C. Lippold and W.F. Savage et. al. (1979) supported the idea of a diffusionless massive transformation.

The other school of thought disagreed with the idea of a massive diffusionless transformation and proposed that there exists a solid-state diffusion upon solidification of ferrite as it cools down to room temperatures (Leone and Kerr, 1982). Leone and Kerr acknowledged the presence of a solid-state diffusion transformation of ferrite ( $\delta$ ) to austenite ( $\gamma$ ) in which Ni diffuses in ferrite towards the advancing austenite while Cr is rejected by the advancing  $\delta/\gamma$  interface which explains experimental results showing an enrichment of Ni and depletion of Cr in the austenite. In addition, experiments conducted by Leone and Kerr showed no evidence for massive or martensitic transformations in the alloys studied. Although these two ideas of austenite transformation mechanism are quite contradictory, it is still clear that both transformations models identify composition and cooling rates as the major driver for the  $\delta \rightarrow \gamma$  transformation.

The solidification mode of austenitic stainless steel can be divided into four types according to the value of  $Cr_{eq}/Ni_{eq}$  <sup>[41]</sup>.



Hammar and Svensson [41] suggests:

$$\text{Cr} = \text{Cr} + 1.37\text{Mo} + 1.5\text{Si} + 2\text{Nb} + 3\text{Ti} \quad (13)$$

$$\text{Ni}_{\text{eq}} = \text{Ni} + 22\text{C} + 14.2\text{N} + 0.31\text{Mn} + \text{Cu} \quad (14)$$

By substituting the compositions from Table 3.1 below into Equations (13) and (14), their  $\text{Cr}_{\text{eq}}$  and  $\text{Ni}_{\text{eq}}$  can be calculated. Therefore;  $\text{Cr}_{\text{eq}} = 19.2209$  and  $\text{Ni}_{\text{eq}} = 12.9760$ ; and the  $\text{Cr}_{\text{eq}} / \text{Ni}_{\text{eq}} = 1.48$ . So that the solidification mode is;

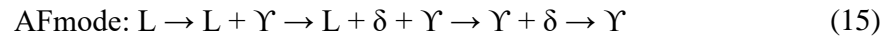


Table 3.1. Material Properties of 304L-Stainless Steel

Material	% Compositions
Fe	Balance
Cr	18
C	0.02
Ni	12
Mo	0.07
Mn	1.7
Si	0.75
S	0.03
P	0.045



From Equation (15) we notice  $\gamma + \delta \rightarrow \gamma$  from the AFmode determines the phase of the end product. Although  $\gamma + \delta \rightarrow \gamma$  predicts austenite as the only phase in the end product, this in reality will depend on the cooling rate such that the final products can also contain fractions of BCC as will be shown subsequently. The phase fractions of austenite ( $\gamma$ ) will provide an idea of the cooling rate that best retains austenite and suppresses ferrite ( $\delta$ ). The goal is then to simulate different ABAQUS models until we obtain one for which the cooling rate matches the cooling rate that produces the most austenite phase fraction from the MatCalc simulation.

**3.2.2. Results from MatCalc.** The Fe-Cr-Ni ternary alloy was used because these three elements are key actors in the phase transformation of stainless steel. Simulating with the entire material compositions does account for contributions from other alloying elements; however, their contributions are relatively small compared to contributions from Fe, Cr and Ni and was ignored in this study.

The procedure for running the diffusional transformation via MatCalc involves:

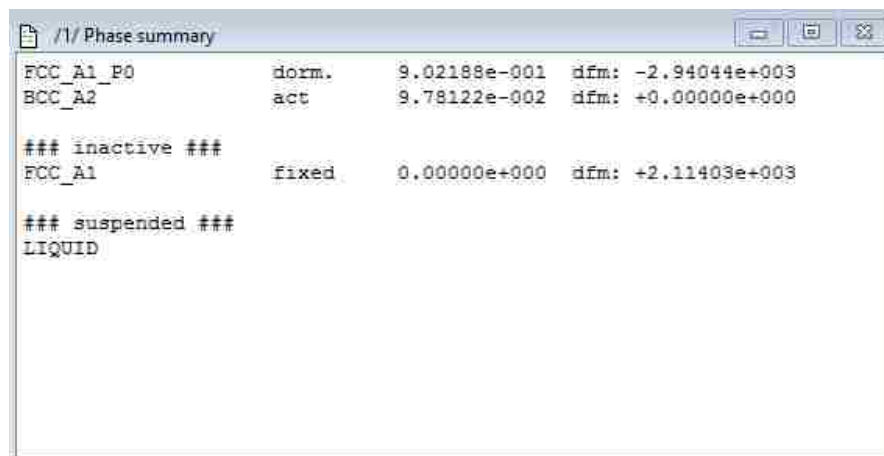
- (a) Selecting the thermodynamic and kinetic database
- (b) Defining the material, % material composition and the anticipated phases that can be present for the given ternary alloy. MatCalc can predict the anticipated phases by running a step equilibrium calculation. Using the information from the step equilibrium, a precipitation domain where the matrix phase (i.e. BCC in this case) and the precipitate phase FCC is selected. By selecting the matrix and precipitate domain as stated, the fractions of FCC precipitated from BCC is captured and added to the original FCC present in the solid solution. The MatCalc software also allows the user to specify temperature ranges so that only phases within the specified temperature ranges are modeled.
- (c) Next, the cooling rates are specified with the time and duration that the process runs until cooled to room temperature. With all the following steps completed, the simulation is ready

to run. Lots of information can be obtained from the simulation results. However, only the phase fractions of FCC and BCC formed were considered. The cooling rates used in the MatCalc simulation were;

- i. 5000 C/s
- ii. 10000C/s
- iii. 20,000 C/s
- iv. 50,000 C/s
- v. 100,000 C/s
- vi. 200,000 C/s
- vii. 500,000C/s
- viii. 1,000,000C/s

The MatCalc simulation was performed for the ternary Fe-Cr-Ni alloy with the composition listed in Table 3.1.

Figures 3.4 to 3.19 show MatCalc results for the phase fractions of ferrite( $\delta$ ) and austenite ( $\gamma$ ) for various cooling rates in a Fe-Ni-Cr alloy for 304L-SS.



Phase	Status	Fraction	dfrm
FCC_A1_P0	dorm.	9.02188e-001	-2.94044e+003
BCC_A2	act	9.78122e-002	+0.00000e+000
### inactive ###			
FCC_A1	fixed	0.00000e+000	+2.11403e+003
### suspended ###			
LIQUID			

Figure 3.4. Phase Fractions Present in Fe-Cr-Ni for the Cooling Rate 5000C/s

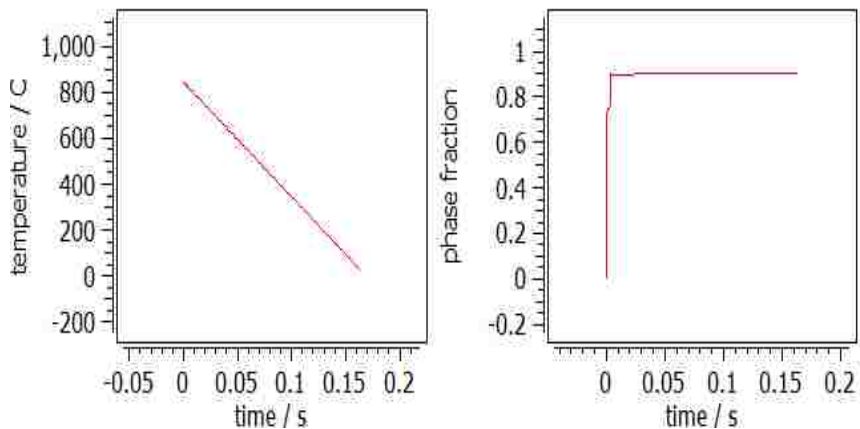


Figure 3.5. Cooling Rate Curve and FCC Phase Fraction-Time Curve at 5000C/s for 304L-SS

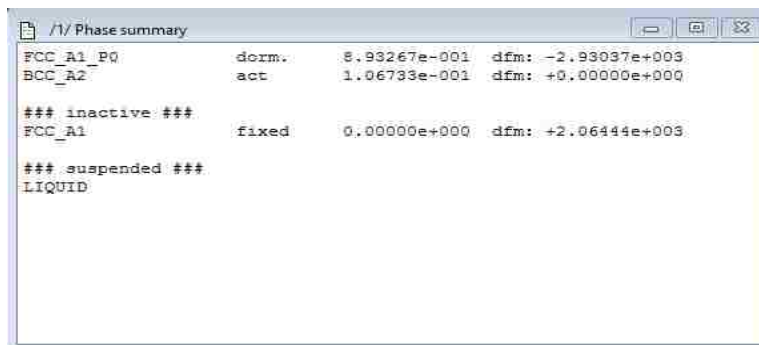


Figure 3.6. Phase Fractions Present in Fe-Cr-Ni for the Cooling Rate 10000C/s

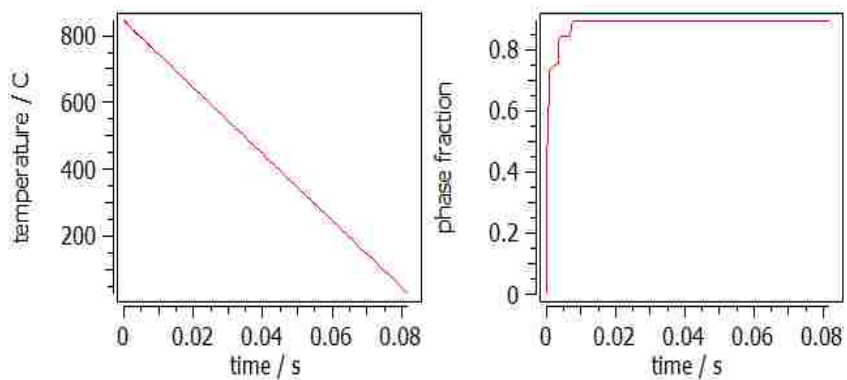


Figure 3.7. Cooling Curve and FCC Phase Fraction-Time Curve at 10000C/s for 304L-SS

/1/ Phase summary			
FCC_A1_P0	dorm.	7.65057e-001	dfm: -2.86278e+003
BCC_A2	act	2.34943e-001	dfm: +0.00000e+000
### inactive ###			
FCC_A1	fixed	0.00000e+000	dfm: +9.29283e+002
### suspended ###			
LIQUID			

Figure 3.8. Phase Fractions Present in Fe-Cr-Ni for the Cooling Rate 25000C/s

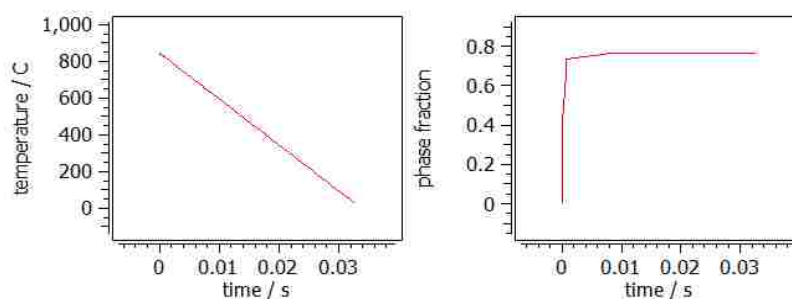


Figure 3.9. Cooling Curve and FCC Phase Fraction-Time Curve at 25000C/s for 304L-SS

/1/ Phase summary			
FCC_A1_P0	dorm.	7.51461e-001	dfm: -2.90057e+003
BCC_A2	act	2.48539e-001	dfm: +0.00000e+000
### inactive ###			
FCC_A1	fixed	0.00000e+000	dfm: +2.23731e+003
### suspended ###			
LIQUID			

Figure 3.10. Phase Fractions Present in Fe-Cr-Ni for the Cooling Rate 50000C/s

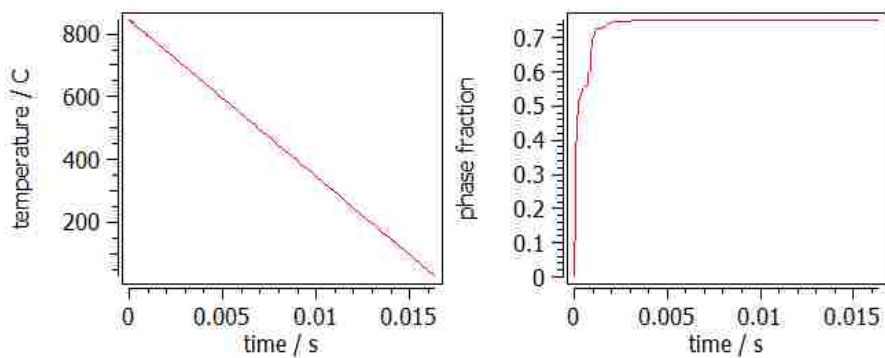


Figure 3.11. Cooling Curve and FCC Phase Fraction-Time Curve at 50000C/s for 304L-SS

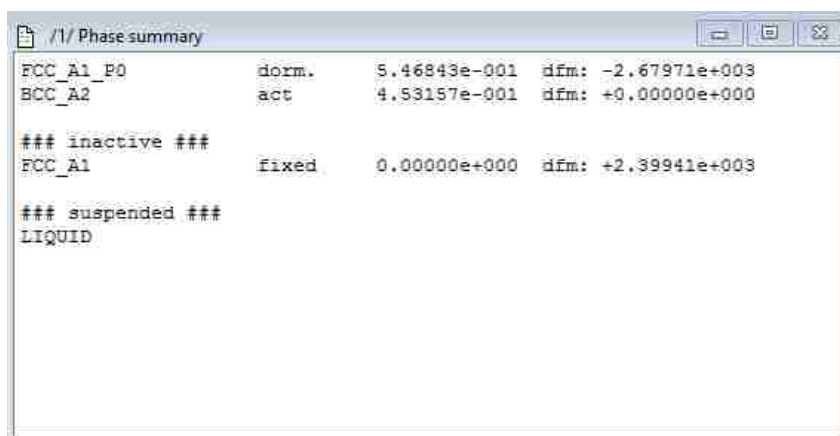


Figure 3.12. Phase Fractions Present in Fe-Cr-Ni For the Cooling Rate 100000C/s

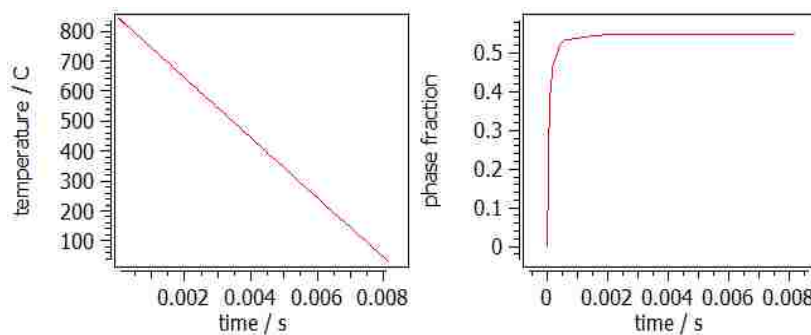


Figure 3.13. Cooling Curve and FCC Phase Fraction-Time Curve at 100000C/s for 304L-SS

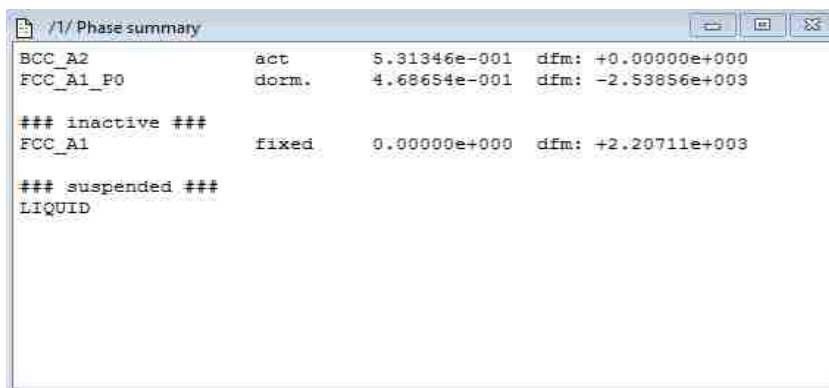


Figure 3.14. Phase Fractions Present in Fe-Cr-Ni for the Cooling Rate 200000C/s

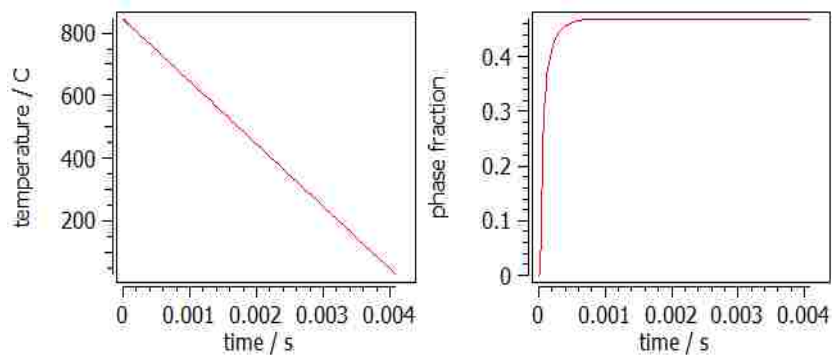


Figure 3.15. Cooling Curve and FCC Phase Fraction-Time Curve at 200000C/s for 304L-SS

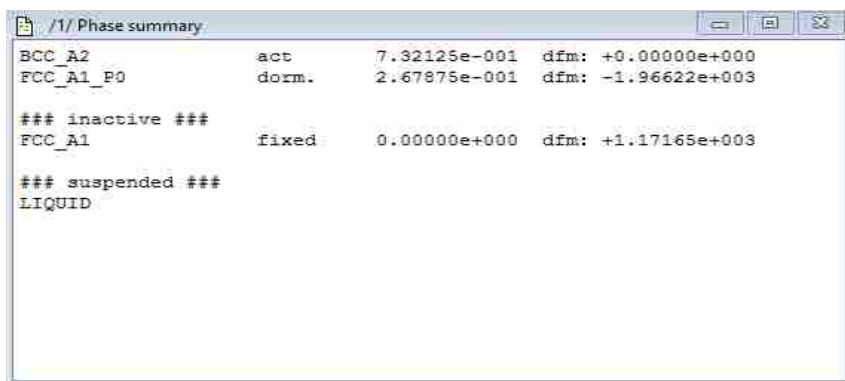


Figure 3.16. Phase Fractions Present in Fe-Cr-Ni For the Cooling Rate 500000C/s

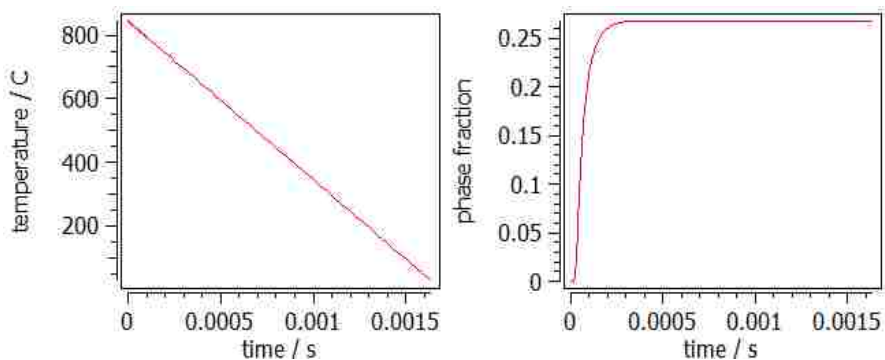


Figure 3.17. Cooling Curve and FCC Phase Fraction-Time Curve at 500000C/s for 304L-SS

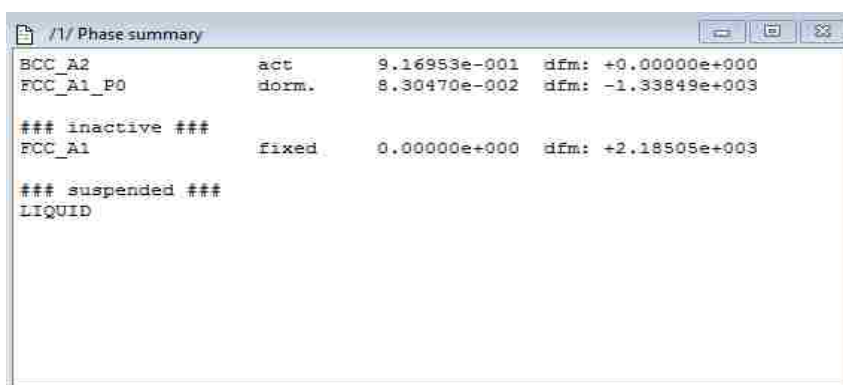


Figure 3.18. Phase Fractions Present in Fe-Cr-Ni for the Cooling Rate 1000000C/s

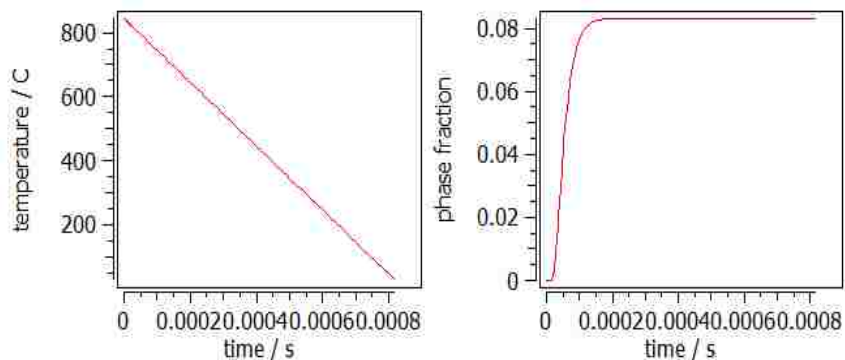


Figure 3.19. Cooling Curve and FCC Phase Fraction-Time Curve at 1000000C/s for 304L-SS

Table 3.2 shows extrapolated values of FCC and BCC phase fractions from Figures 3.4 to 3.19.

Table 3.2. Phase Fractions of FCC in Fe-Cr-Ni for Different Cooling Rates via MatCalc

Cooling rate (C/s)	FCC fraction	BCC fraction
5000	9.02E-1	9.78E-2
10000	8.93E-1	1.07E-1
25000	7.65E-1	2.35E-1
50000	7.51E-1	2.48E-1
100000	5.47E-1	4.53E-1
200000	5.31E-1	4.69E-1
500000	2.68E-1	7.32E-1
1000000	8.30E-2	9.17E-1

Figure 3.20 shows that BCC phase is dominant at very high cooling rates (>150,000C/s) while FCC phase dominates at lower cooling rates (<150,000C/s). The cooling gradient is very high at the start of cooling and certainly not a straight curve. Therefore, in the cooling process, there will be areas in which the cooling rate favors BCC phase and others in which the cooling rate favors FCC depending on the input power.

Temperature is also an important factor to consider here since phase transformation will usually begin and end within a temperature band. It is therefore important to note the temperature range where the bulk of the phase transformation will most likely begin and end. A good estimate of the temperature range comprising most of the phase transformation activity can be obtained from MatCalc and is shown Figure 3.21 below.



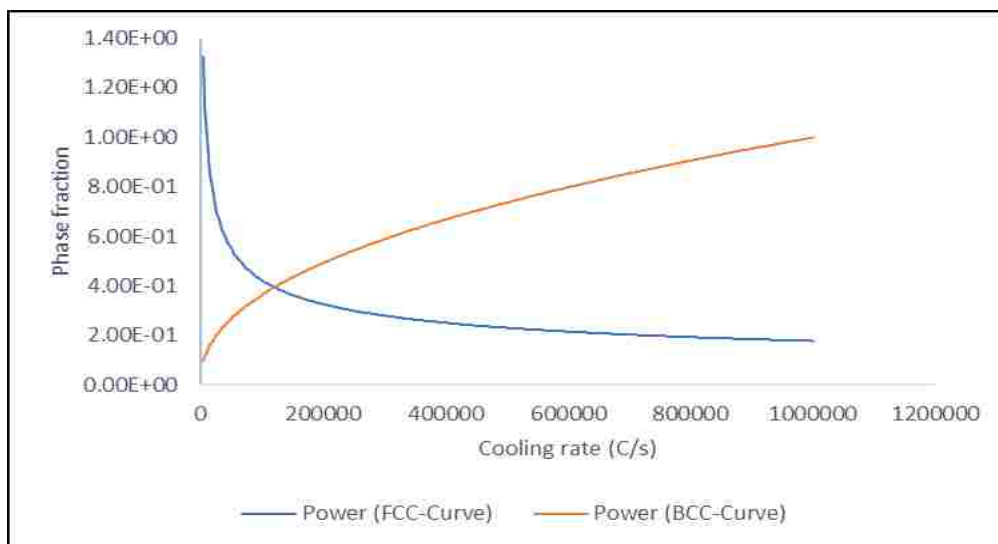


Figure 3.20. Cooling Rates for FCC vs BCC Phase Fractions on Fe-Cr-Ni Alloy in 304L-SS

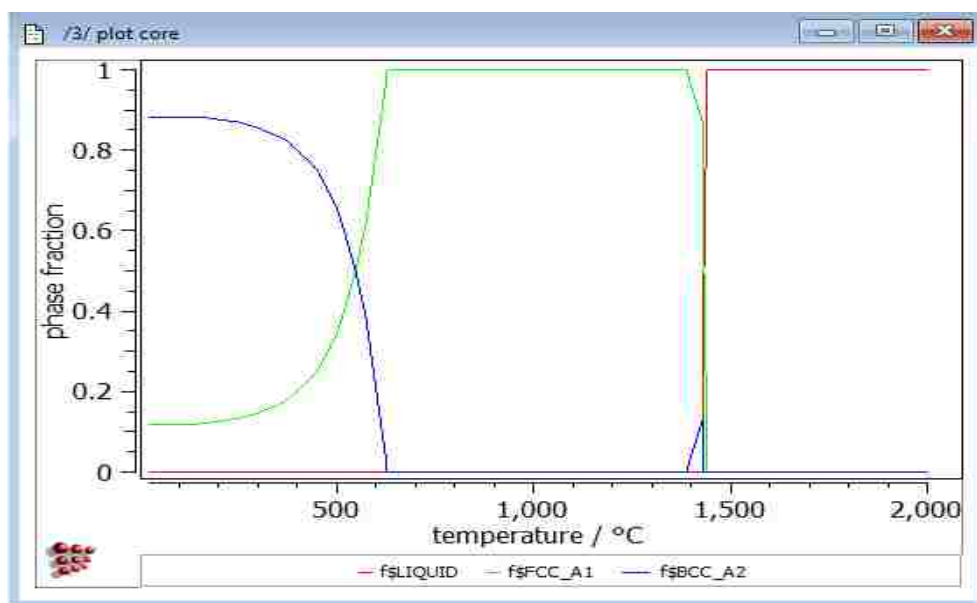


Figure 3.21. Generic Phase Diagram of Fe-Cr-Ni (304L-SS) Showing Possible Phases and their Corresponding Temperature Ranges

From Figure 3.21 it can be seen that the temperature range at which FCC and BCC co-exist lies between 625°C (i.e. ~900K) to 125°C (i.e. ~ 450K). Below 450K from Fig. 3.21,

the phase fractions of FCC and BCC is constant indicating complete phase transformation. Above 900K, only the FCC phase is present. Hence this range 900K – 450K accounts for majority of the phase transformation observed and ultimately determines the phases and the respective phase fractions of the consolidated material.

#### 4. FINITE ELEMENT ANALYSIS

ABAQUS CAE 2016 was used to simulate the finite element model. The schematic of the SLM process setup is shown in Fig. 4.1 below. The substrate and the powder bed are made of the same material (i.e. 304L SS). The substrate acts as a base support for the build part and was 0.000225m thick while each powder layer was 50 $\mu$ m thick. Pulsed laser scan was used for this experiment where the laser beam was held at a fixed spot on the powder bed for a certain time period. The time duration for each model depended on the laser power. From investigations based on several trials, a time duration of 75 $\mu$ sec was sufficient for a through thickness melt pool of laser powers greater than 100W while 0.02secs was needed for laser powers  $\leq$  50W. Simulation investigations show that a total of four laser spots on a single laser track (each spaced 50 $\mu$ m apart) was sufficient to account for effects like thermal field interference from neighboring heated points. Results from the third and fourth laser points showed consistency with experimental results and converges to almost same thermal profile after the third laser pulse. Hence the thermal profile for the third laser spot was chosen in this study as a reference. This means that simulation dimensions for melt pool depth and width and the thermal profiles over the melting and cooling periods was taken from the results of the third laser pulse simulation.

The material properties of the powder bed were partitioned into two field variables (1 and 0) in ABAQUS to account for the differences in temperature dependent material properties between the 304L-SS liquid and solid 304L-SS during melting and consolidation, which is quite significant. The transition between powder to liquid is controlled by the solidus point 1673K. Thus, upon heating the material is considered powder and follows the user-defined temperature dependent material properties data for 304L-SS powder in ABAQUS until  $>1673$ K where the material properties data switches to the user-defined

material properties for molten 304L-SS. When the material cools down, the material properties data simply follow the user-defined temperature dependent material properties data of a solid 304L-SS. The temperature dependent properties include: specific heat, conductivity and density and can be obtained from experimental tables if available or from available empirical formula which was used in this study.

A fixed boundary condition at the base edges of the substrate in all directions was implemented to maintain structural integrity from movements due to forces evolving from thermal gradients and viscous forces during the SLM process simulation. The initial temperature before simulation was 300K. Other parameters like film coefficient (20) and emissivity (0.7) were applied to the ABAQUS model powder to account for convection and radiation interactions. The load was applied through a user-defined subroutine (see Appendix B for details). A simulation time step of 25 $\mu$ sec was sufficient to predict accurate results. A standard 3D linear Hex C3D8T element (8-node thermally coupled brick trilinear displacement and temperature element) was selected for meshing purposes. The ABAQUS output results can be either viewed as graphic image or as a table or graph. Animated graphics is also available showing how the process evolves over the entire time domain.

#### **4.1. ABAQUS MODEL SIMULATION**

This section of the report has made efforts using ABAQUS software to model the SLM process to produce cooling rates almost identical to the cooling rates in the MatCalc simulation. The ABAQUS model consists of a powder layers of thickness 50 $\mu$ m supported by a substrate block of same material (304L-SS). For obtaining only the cooling rates, a single pulse laser scan is sufficient since subsequent laser scans will produce similar cooling curves. However, for measuring the melt pool depth and width, three laser points was simulated to account for thermal effects from neighboring melt pool. The laser pulse duration

was selected carefully to allow sufficient time for through thickness melt pool (i.e. melt pool depth  $\geq 50\mu\text{m}$ ). This is determined by the time it takes the temperature at the bottom of the powder layer to rise above the liquidus temperature ( $\sim 1750\text{K}$ ). Once this is achieved, the laser pulse stops and the material is allowed to cool down to a steady or constant temperature and the cooling curve extracted from the ABAQUS output file.

#### 4.2. GENERAL PROCESS SETUP

The heat modeling in SLM is a complex transient analysis involving a number of time and temperature dependent coupled-partial differential equations. Several books and papers have been written on time and temperature dependent heat transfer and will be utilized in this research to model the SLM temperature profile. Some of these equations will be used to create a subroutine that simulates the heat flux in ABAQUS while other equations will be used to generate temperature dependent material properties that will be directly entered into ABAQUS. Figure 4.1 illustrates an SLM process setup.

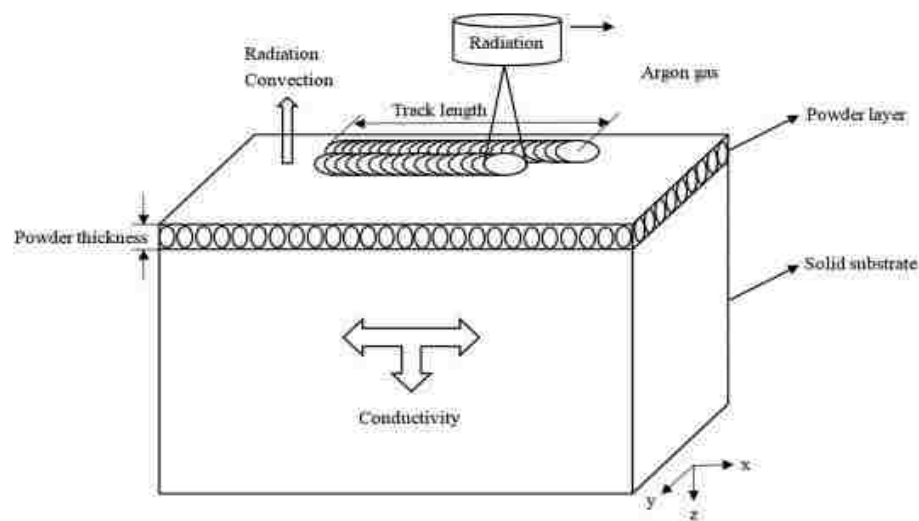


Figure 4.1. Schematic of SLM Process Setup [44]

The powder bed, although depicted as a metal slab resting on the top surface of the substrate is actually a layer of metallic powder particles (i.e. 304 L- stainless steel powder) spread evenly onto the surface of the substrate by the powder deposition unit. After each powder layer is completely scanned, the powder bed is lowered and fresh powder layer from the feed container is deposited onto the previously scanned layer and the process repeats until the part is built. The laser beams from the laser equipment (i.e. Renishaw 250 AM 200W fiber laser) is directed to the build platform (250 X 250 X 300mm build volume) with the help of the mirror scanner and the  $f-\theta$  lens. The build chamber is a fully welded vacuum for low pressure evacuation, filled with argon inert gas and keeps oxygen concentrations below 50ppm through low gas consumption to enable safe use of reactive metals which also allows for better overall mechanical performance (<http://www.renishaw.com/en/am250--15253>). The Renishaw 250AM is capable of printing  $20\mu\text{m}$  to  $100\mu\text{m}$  thick layers of fully dense metal directly from a 3D CAD program.

As the laser hit the surface of the powder bed, the metal powder absorbs radiant energy from the beam, reflects some energy and conducts most energy to neighboring powder particles, while some energy is lost through evaporation. Of course, as the powder bed is irradiated, its temperature increases accordingly. If the intensity of the laser beam and time of exposure is sufficient enough, this increase in the powder bed temperature reaches solidus (i.e. 1697K for 304L-SS) above which the powders begin to melt into liquid metal. This transition point between solid powder-to-liquid metal is very critical to a more realistic model of the heat transfer process due to latent heat. The powder is fully melted into a liquid pool at the liquidus temperature (i.e. 1727K for 304L-SS). Conversely when the laser goes out or is stopped (i.e. for a pulsed laser beam) or transitions further away (i.e. for a moving laser beam) the temperature of the molten pool falls below the liquidus and the solidification

process begins until a solid structure is formed. In order to capture the different changes occurring during the SLM process; the model is categorized into three stages (i.e. pre-heating, melting and re-solidification) and the changes evolving during the process i.e. conduction, heat flux, absorption, evaporation, latent heat, etc. are discussed in the applicable stages of the model. These changes mentioned above are needed to effectively model the SLM process and ensure the model developed is a fairly accurate representation of the true process.

### **4.3. PROCESS MODEL**

There are several properties that significantly affect and control the temperature gradient and thermal effects observed during melting and cooling. The most notable ones being specific heat, conductivity and density which are all temperature dependent. Temperature dependent properties for conductivity, density and specific heat exists for some material obtained from experiments. However, an effort is being made in this study to derive these properties using some standard formula. Other properties such as radiation, emissivity, absorptivity and surface convection and evaporation are equally important and are accounted for in the ABAQUS subroutine and ABAQUS model setup. The heat flux was modeled using the Goldak heat distribution model. Observations from the simulation results show that non-axisymmetric three-dimensional heat source (i.e. Goldak model) gives better correlation with experimental results compared to the standard 3D Gaussian heat distribution model. Experimental results were compared with the ABAQUS model analysis result and had good agreement. The following subsections discuss these concepts in details.

**4.3.1. Temperature-Dependent Thermal Conductivity.** The preheating stage encompasses the temperature ( $t$ ) range from ambient ( $t_0$ ) up to solidus ( $t_s$ ) i.e.  $t_0 \leq t \leq t_s$ .

Within this temperature range, the powder is still in the solid or unmolten phase and therefore the heat on the powder bed from the laser beam irradiation is transmitted basically by conduction through powder particle contact and also by scattering of radiation field through the gaps between powder particles, giving rise to multiple reflections in the powder bed and consequently to absorptivity values that are substantially higher than in dense materials.

Light scattering by spherical particles is generally described by the Mie theory [45]. According to the Mie theory; matter is composed of discrete particles. When light is incident on a particle, there's an emission of secondary radiation known as scattering. In addition to scattering, part of the incident radiation may be extinguished within the particle provided that it is absorbing i.e. having complex index of refraction. Hence scattering and absorption leads to the temporal implication of reduction of the incident light after traversing a particle, with a net effect of radiation extinction. Whilst Mie theory explains the scattering effect of radiation through the pores spaces, it involves a very complex algorithm and requires Maxwell's equation, ray tracing and Rayleigh approximations to compute, hence it is only mentioned here as reference. A rather different approach is adopted for this research.

To simplify the model and reduce its computational ambiguity, the powder bed is assumed to be a solid metal rather than powder. An effective thermo-mechanical set of equations are then used to obtain approximate values of the true properties of the metallic powder. For a thermo-mechanical coupled system, the thermal equilibrium equation for heat transfer [46], [47] can be written as;

$$K \left( \frac{\partial^2 T}{\partial x^2} + \frac{\partial^2 T}{\partial y^2} + \frac{\partial^2 T}{\partial z^2} \right) + q = \rho C T + v \frac{\partial T}{\partial z} \quad (16)$$

Also from H.S. Carslaw et al. [48], the maximum surface temperature induced by a stationary Gaussian beam is;



$$T_0 = \frac{A_{\text{eff}}P}{dK_{\text{eff}}}\sqrt{\frac{2}{\pi}} \quad (17)$$

Where;

d: diameter of laser beam (m)

$A_{\text{eff}}$ : effective heat absorptivity of laser beam on powder surface

$K_{\text{eff}}$ : effective heat conductivity (J/m.s.k)

P: laser power (W)

Several equations are available that can predict the thermal conductivity of powder beds at high temperatures. The two prominent ones include the Yagi-Kunii equation [49] and the Zehner-Schlunder equation [50]. Kunii and Smith developed an expression for the effective thermal conductivity with stagnant fluid based on one dimensional heat diffusion model for a unit cell of packed spheres. The Zehner, Bauer and Schlunder (ZBS) model considered the heat flux assuming parallel heat flux vectors as a unit cell and also accounted for particle shape, radiation effect, fluid pressure dependence, contact conduction, particle flattening, shape and size distribution and oxidation effects using adjustable parameters for particles [51]. This study adopts the ZBS model to determine the thermal conductivity of the powder during heat transfer. The ZBS model equation is as follows:

$$\frac{K_c}{K_f} = (1 - \sqrt{1 - \epsilon}) + \sqrt{1 - \epsilon} \left( \frac{2}{1 - \left(\frac{BK_f}{K_s}\right)} \right) \left[ \frac{\left(1 - \frac{K_f}{K_s}\right) B}{\left(1 - \left(\frac{K_f}{K_s}\right) B\right)^2} * \ln\left(\frac{K_s}{K_f B}\right) - \frac{B-1}{2} - \frac{B-1}{1 - \left(\frac{K_f}{K_s}\right) B} \right] + (1 - \sqrt{1 - \epsilon}) (K_r/K_f) + \sqrt{1 - \epsilon} \left( \frac{K_f}{K_r} + \frac{K_f}{K_s} \right)^{-1}$$

Where;

$$K_r = 4\sigma \left( \frac{\epsilon}{2 - \epsilon} \right) T^3 D_p$$

$$B = C \left( \frac{1-\epsilon}{\epsilon} \right)^{\frac{10}{9}}$$

$$C = 1.25$$

B: deformation coefficient

C: particle shape factor

$D_p$ : diameter of particle (m)

$K_e$ : effective thermal conductivity of packed bed (W/m·K)

$K_f$ : thermal conductivity of fluid (W/m·K)

$K_r$ : radiative component of effective thermal conductivity (W/m·K)

$K_s$ : thermal conductivity of stainless steel (W/m·K)

$\epsilon$ : void fraction

$\epsilon$ : emissivity

$\sigma$ : Stefan–Boltzmann constant (W/m<sup>2</sup>·K<sup>-4</sup>).

T: temperature (K)

The porosity of the powder bed at ambient temperature (i.e. 300K) is approximately 0.31-0.38. A porosity of 0.35 is adopted for this paper.  $K_g$  (thermal conductivity of continuous gas, i.e. argon) is approximated as 27  $\mu$ W/m. K at 500K and 1bar pressure while  $K_s$  (thermal conductivity of 304L-SS solid flat plate) is approximately 14.89 W/m. K at 300K and 1bar pressure respectively. However, the thermal conductivity is a temperature dependent property and changes significantly as the temperature increases. In order to account for this change in thermal conductivity, two separate linear equations were developed taken from the gradient of the temperature dependent conductivity plot of  $K_g$  and  $K_s$ , from [52] , [53] .

The temperature dependent conductivity graphs for 304L stainless steel and Argon are shown, respectively, in Figures 4.2 and 4.3 below;

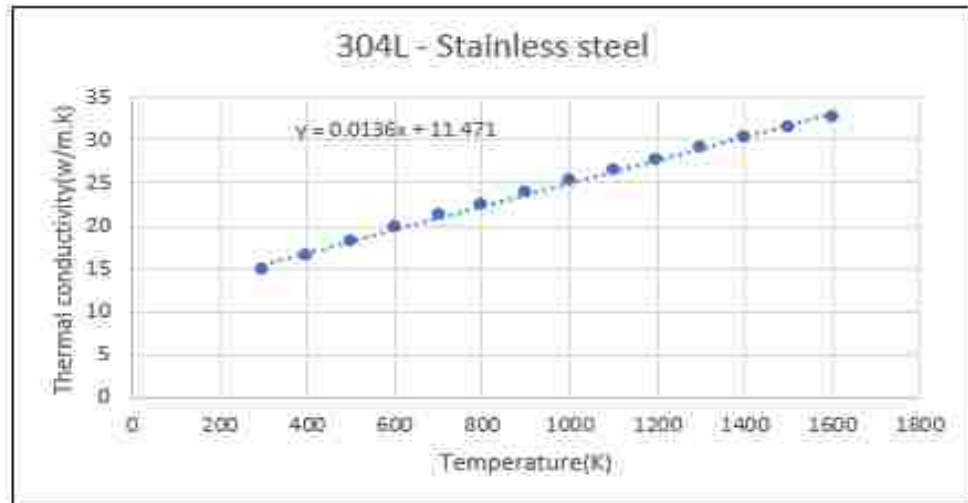


Figure 4.2. Temperature-Dependent Thermal Conductivity Plot for 304L Stainless Steel

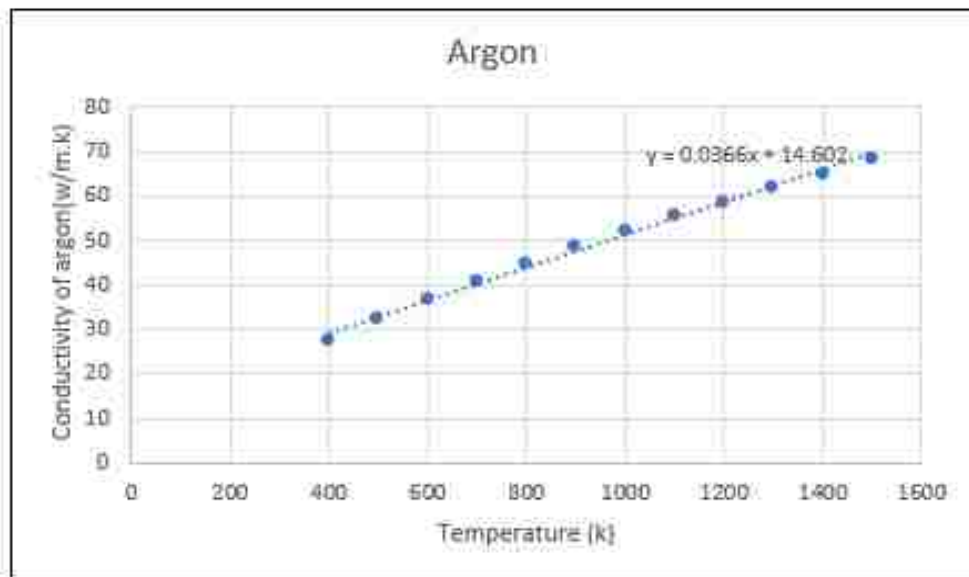


Figure 4.3. Temperature-Dependent Conductivity Plot for Argon

The gradient equation for the temperature dependent conductivity of 304L-SS and Argon are;

$$K_s = 0.0136T + 11.471 \text{ (for 304L-SS from 300K to 1697K)}$$

$K_g = 0.0366T + 14.602$  (for Argon), respectively.

Two other important temperature dependent material properties include density ( $\rho$ ) and specific heat ( $C_p$ ).

**4.3.2. Density.** The density depends on the phase state of the heating process and can be categorized as density at solid state and density at liquid state. From the Law of conservation of mass; it is logical to say that the mass is constant throughout the process assuming we neglect mass losses through evaporation which is insignificant relative to the mass of the solid powder. However, the density is significantly less at liquid state due to an increase in volume as the metal powder melts. The effect of expansion due to increasing temperature is not significant and is ignored. Hence, it is assumed that the density is only affected by a change in state, i.e. from solid to liquid. The density of molten 304L stainless steel is  $7200\text{kg/m}^3$  from [54], and its density at ambient temperature (i.e. at 300K) is  $7900\text{kg/m}^3$ . Therefore, at;

- i. Preheat zone:  $300\text{K} \leq T \leq 1697\text{K}$

$$\text{Density}(\rho) = 7900\text{kg/m}^3$$

- ii. Liquid zone:  $T \geq 1697\text{K}$

$$\text{Density}(\rho) = 7200\text{kg/m}^3$$

**4.3.3. Temperature Dependent Specific Heat.** The temperature-dependent specific heat tables for 304L stainless steel was not available so tables for 316 stainless steel from INCO data-books (“Austenitic chromium-nickel stainless steels Engineering properties at elevated temperatures”) was rather used here as a substitute since both materials possess similar thermal properties. The plot showing the temperature dependent – specific heat is

shown in the Figure 4.4 below. From Figure 4.4; the slope of the specific heat  $C_p = 0.1115T + 470.83$ .

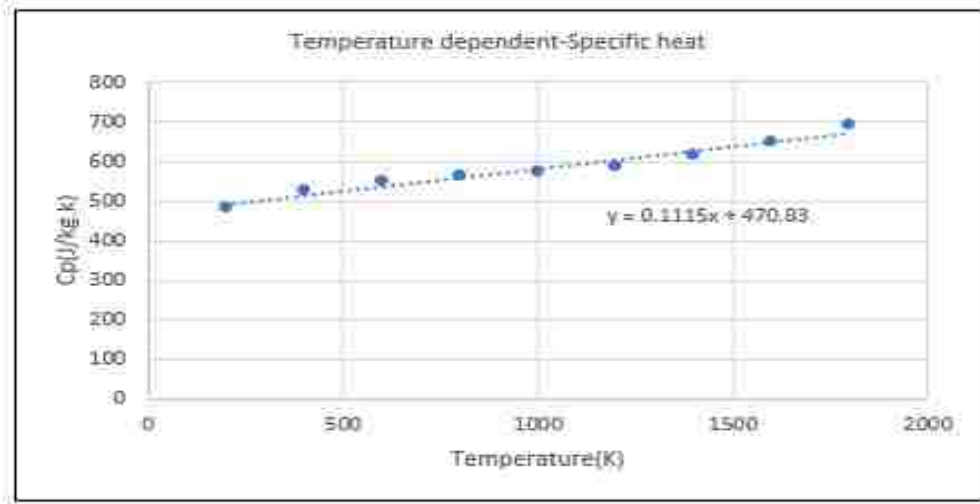


Figure 4.4. Temperature Dependent – Specific Heat Plot for 304L Stainless Steel

#### 4.4. HEAT FLUX DISTRIBUTION

Although the 3D Gaussian heat distribution is still a very common method for calculating heat flux distribution, several researches have shown that it's results can be misleading for temperatures in or near the fusion and heat-affected zone (Goldak et al; 1984). A non-axisymmetric three-dimensional heat source (Goldak et al., 1984) was used in this investigation. It is argued on the basis of molten zone observations that this is a more realistic model and more flexible than most other models proposed for weld heat sources. It is capable of predicting shallow and deep penetration welds and can accommodate asymmetrical situations as well. Goldak heat source:

$$q(x, y, z, t) = f(f, r) \frac{6\sqrt{3}.Q}{abc\pi\sqrt{\pi}} .e^{-\frac{3x^2}{a^2}} .e^{-\frac{3y^2}{b^2}} .e^{-\frac{3z^2}{c^2}}$$

Where

$$Q = PE$$

P: laser power

E: laser efficiency (1 for pulsed laser)

$f(f, r) = 1.4$  was used in this study (Bonifaz et al. (2000), suggested  $f(f, r) = 0.6$  to 1.4).

a and b represents the dimensions in the major and minor axis of the consolidated bead.

c is a function that relates with the melt pool depth.

To obtain approximate values of a, b and c, an SLM experiment was performed using laser powers 100W, 150W and 200W with a point distance of 40 $\mu$ m, 60 $\mu$ m and 80 $\mu$ m respectively. This experiment was conducted by Cody Lough (Dept. Mechanical engineering, Missouri S&T, 2017) and the results and are discussed next.

**4.4.1. Metallographic Images.** All images in this section were taken with the Hirox microscope of polished line scans structures etched with 60-40 nitric acid. Figure 4.5 shows an unexpected spherical shape of a line scan built on top of the last layer as a result of discontinuous melting.

In order to measure the depth and width of the melt pool, a cut section along the major diameter comprising three laser scans on three powder layers was made, and the averages of their heights and lengths measured corresponds to the depth and width of the melt pool or consolidated metal powder. Figures 4.6 through 4.8 show examples of the measured width and depth of melt for laser powers 100, 150, and 200 W respectively, while Figures 4.9 and 4.10 show the graph of the melt pool width and depths for the various laser power inputs.

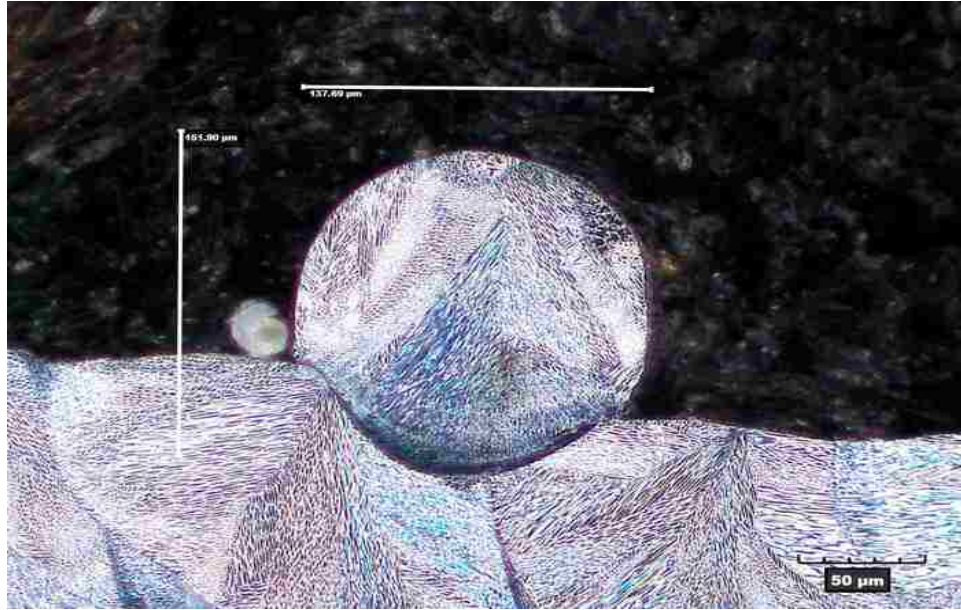


Figure 4.5. Line Scan on Last Layer with Laser Power 200W and Point Distance 60 μm

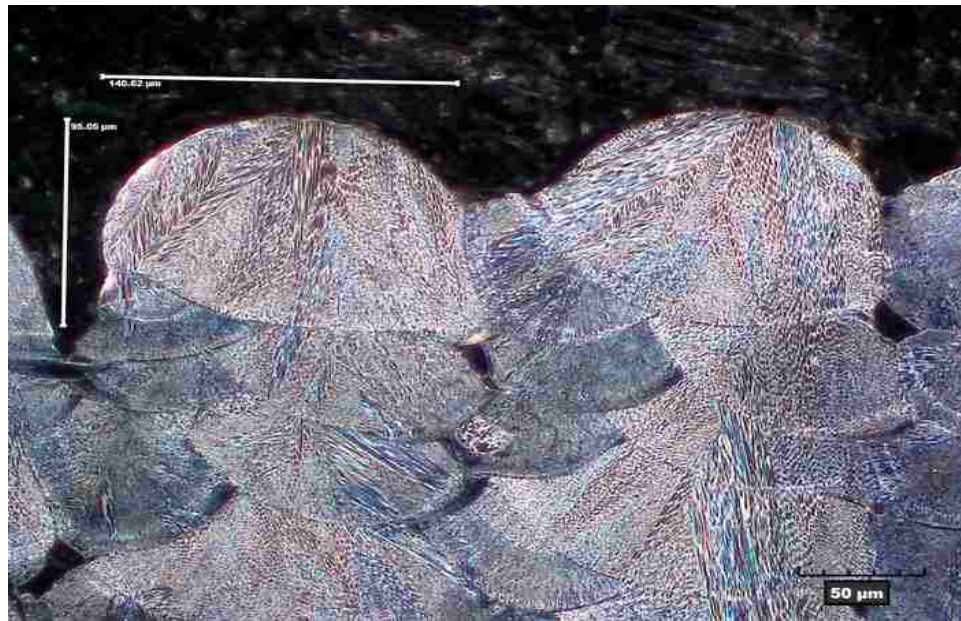


Figure 4.6. Top Layers of Structure Built with Laser Power 100W and Point Distance 60 μm



Figure 4.7. Top Layers of Structure Built with Laser Power 150W and Point Distance 60µm

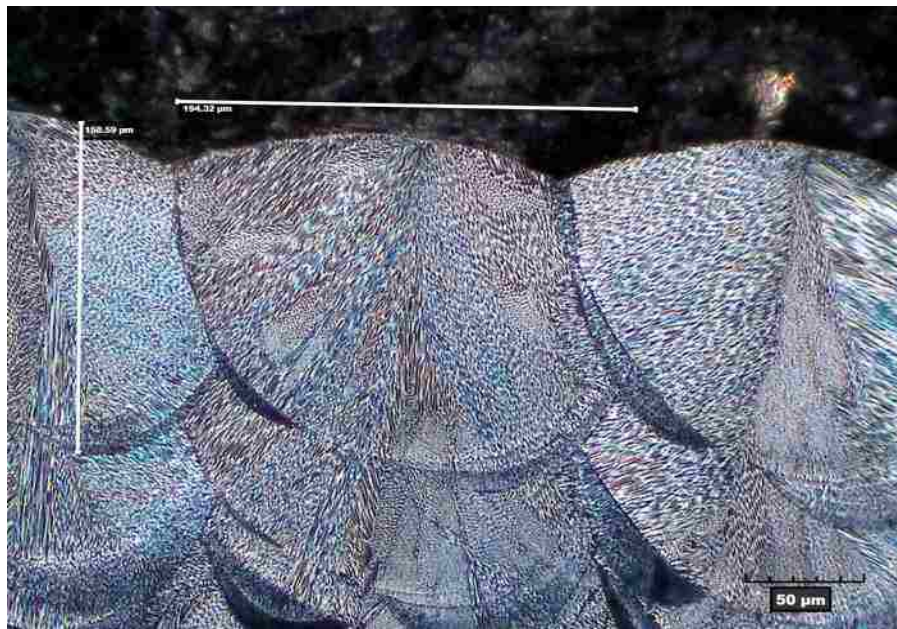


Figure 4.8. Top Layers of Structure Built with Laser Power 200W and Point Distance 60µm



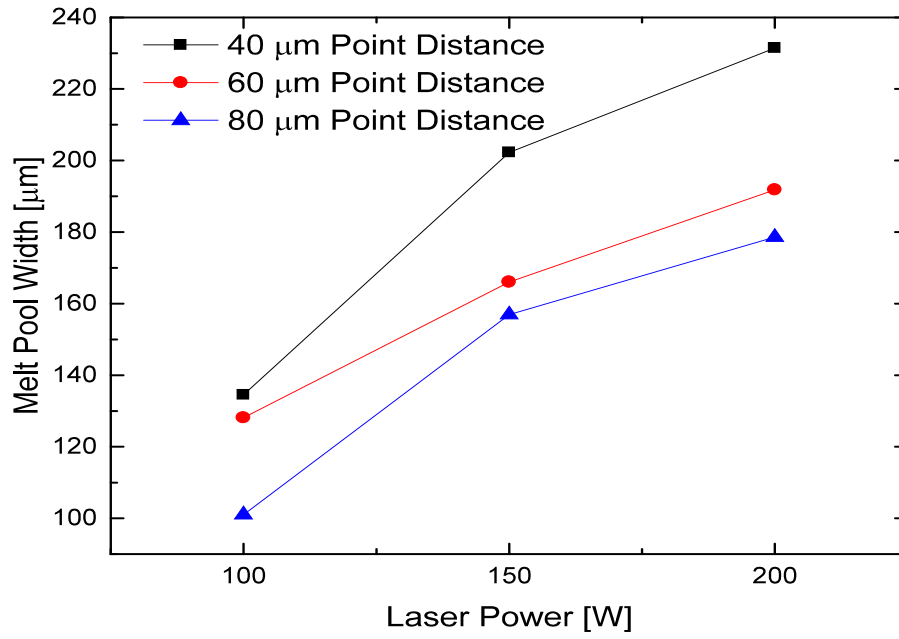


Figure 4.9. Experimental Melt Pool Width

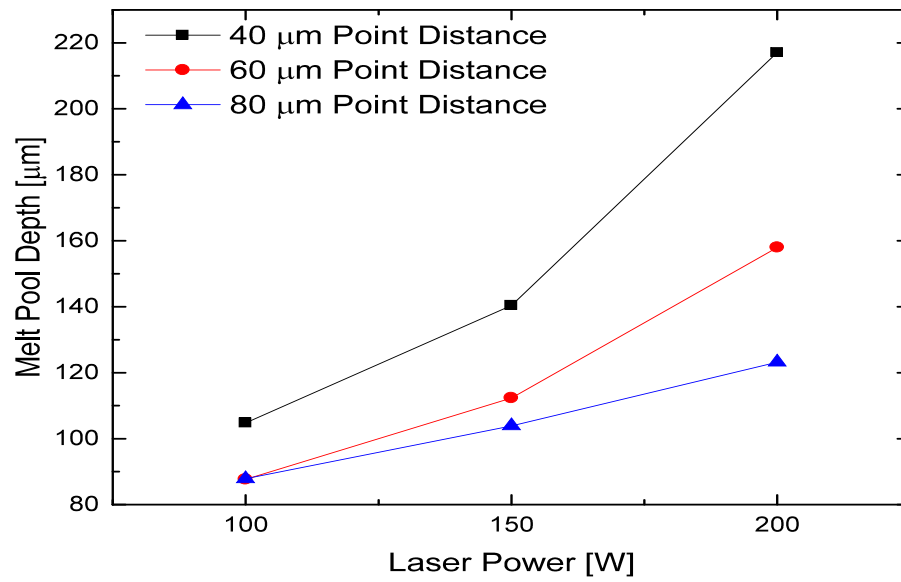


Figure 4.10. Experimental Melt Pool Depth

For sake of convenience, the ABAQUS model was developed using a point distance of 40 $\mu\text{m}$ . Tables 4.1 and 4.2 show the melt pool widths and melt pool depths for the various laser powers at 40 $\mu\text{m}$  laser point distance, extrapolated from the Figures 4.9 and 4.10 respectively.

Table 4.1. Experimental Melt Pool Width for a 40 $\mu\text{m}$  Point Distance

Laser power (W)	Melt pool width ( $\mu\text{m}$ )
100	135
150	205
200	230

Table 4.2. Experimental Melt Pool Depth for a 40 $\mu\text{m}$  Point Distance

Laser power (W)	Melt pool depth ( $\mu\text{m}$ )
100	105
150	140
200	220

The shape of the solidified melt pool from Figures 4.5 to 4.8 resembles an ellipse. It's minor and major axis lengths can be derived mathematically from Equations (18) and (19) below, where a, b and f were as defined in Figure 4.11.

Typically, the relationship between the major and minor axis of an ellipse can be represented mathematically as;

$$\text{Minor axis } (M_a) = \sqrt{(a+b)^2 - f^2} \quad (18)$$

$$\text{Major axis } (M_j) = a + b \quad (19)$$

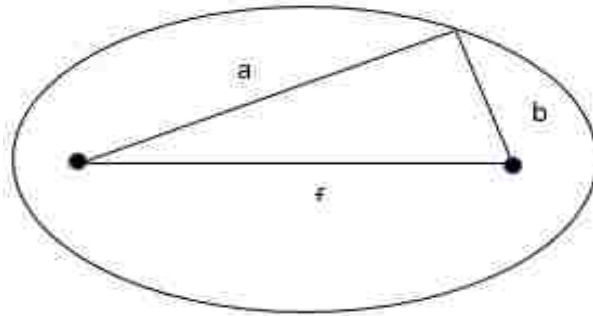


Figure 4.11. An Ellipse with Focal Points Indicated by the Black Dots

$a$ ,  $b$  are the distances from each focus to any point on the ellipse and  $f$  is the distance between foci. Equation (18) can be re-written as;

$$M_n = \sqrt{M_j^2 - f^2} \quad (20)$$

$M_j$  is the width of the bead from the experiment. If we assume  $f$  is  $5/7$  of  $M_j$ , then we can easily obtain  $M_n$  from Equation (20) by mere substitution. The results for  $M_n$  is shown in Table 4.3 below.

Table 4.3.  $M_n$  for Different Laser Powers

Laser power (W)	$M_n$ ( $\mu\text{m}$ )
100	94.48
150	143.47
200	160.97

$$a = 0.5 * M_j \quad (21)$$

$$b = 0.5 * M_n \quad (22)$$

c = Melt pool depth from Table 4.2

Table 4.4 shows values of a and b for the laser powers obtained from Equations (21) & (22).

Table 4.4. a and b for Different Laser Powers

Laser power (W)	a (μm)	b (μm)
100	67.5	47.24
150	102.5	71.74
200	115	80.49

Using values a, b and c from Table 4.2 and 4.3, the heat distribution and temperature profile for the SLM model is simulated via ABAQUS. To account for other uncertainties such as laser efficiency, surface effects, etc. a correction factor was introduced into the Goldak heat flux equation to bring the simulated result as close as possible to the measured value. After several rigorous trial and error using the experimental values as a reference, the following correction factors was adopted for the penetration depth and heat flux distribution.

- Penetration Depth: Apply a correction factor of  $[e (44.7236/\text{laser power})]$ ; i.e. for 200W, 150W and 100W the correction factors for the penetration depths are 1.25, 1.347 and 1.564 respectively.
- Heat Flux Distribution: Apply a correction factor of  $[0.0037719 \times \text{laser power}]$  i.e. for 200W, 150W and 100W the correction factors for the heat flux distribution are 0.75439, 0.56579 and 0.37719 respectively.

**4.4.2. ABAQUS Output Graphic.** The figures below (Figures 4.12 to 4.17) show the ABAQUS output results for the SLM simulations with the various power inputs. The two red dots indicate the measurement node points. The two red dots on the surface of the powder bed that runs horizontally on the x-y plane represents the melt pool width at the end of the laser pulse. These points (red dots) also shows the boundary or contour with minimum temperature above 1727K (melting point of 304L-SS), indicating a molten region. Red dots along the vertical plane through the powder surface indicates the melt pool depth. The values of the melt pool width and depth is displayed in the “Base distance” field at the bottom of the graphic under “magnitude.”

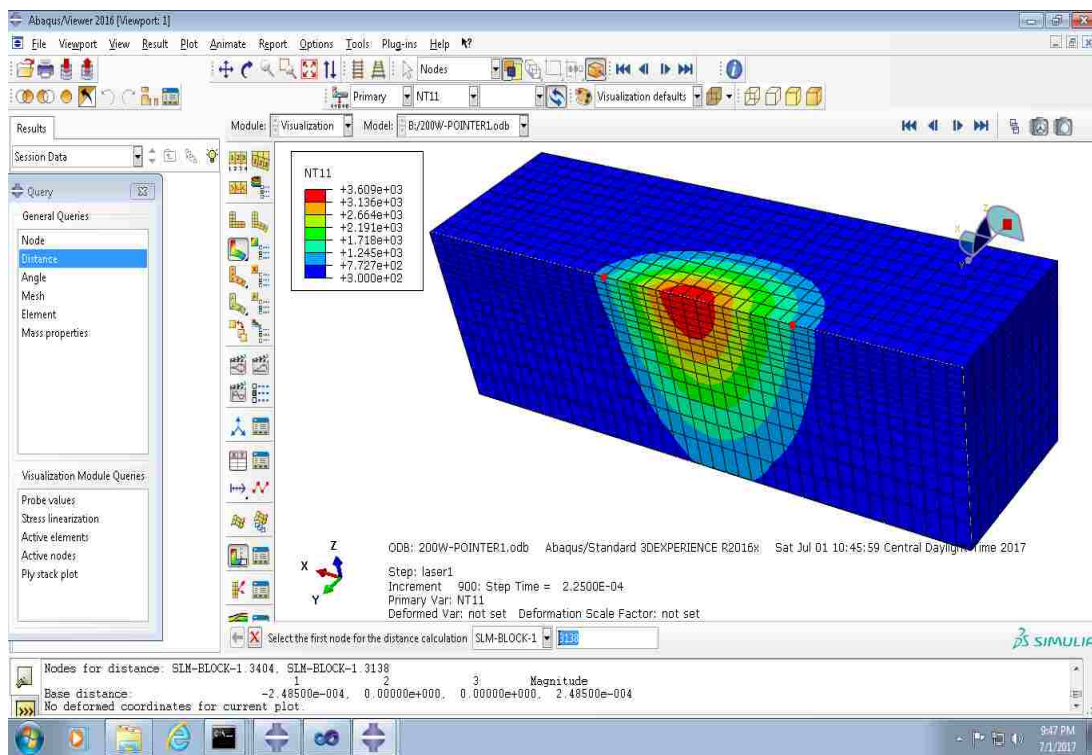


Figure 4.12. Melt Pool Width for 200W Laser Power (248 $\mu$ m)

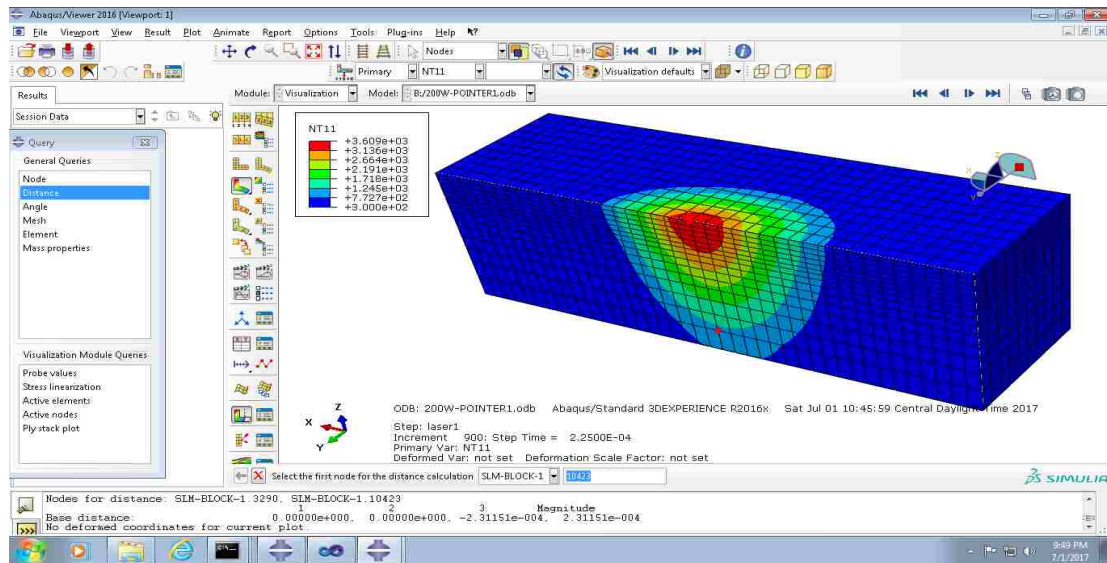


Figure 4.13. Melt Pool Depth for 200W Laser Power ( $231.1\mu\text{m}$ )

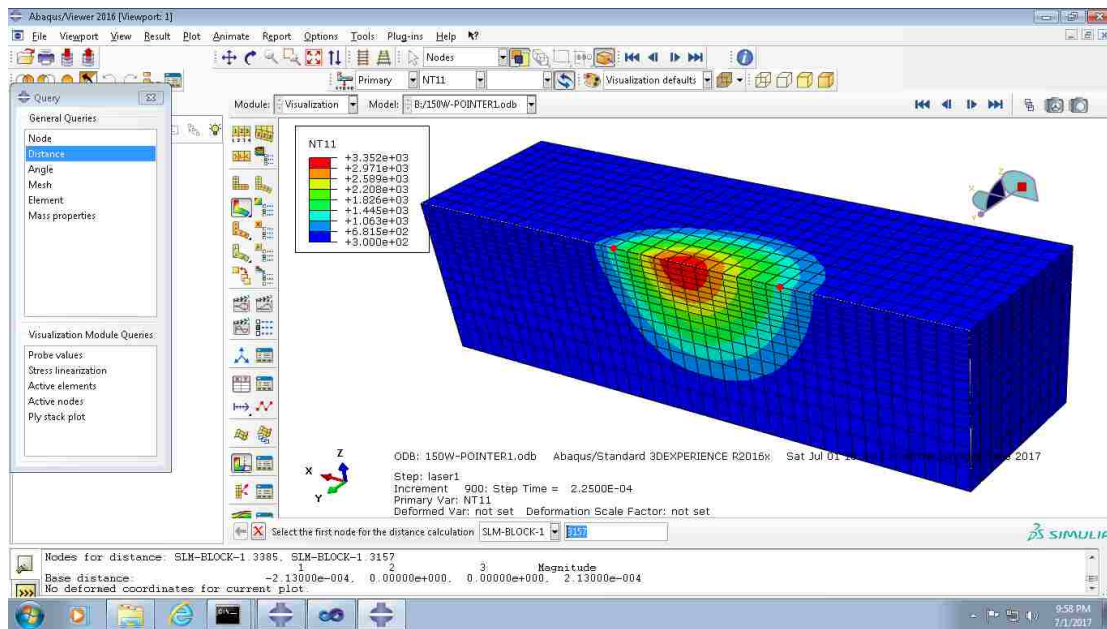


Figure 4.14. Melt Pool Width for 150W Laser Power ( $213\mu\text{m}$ )

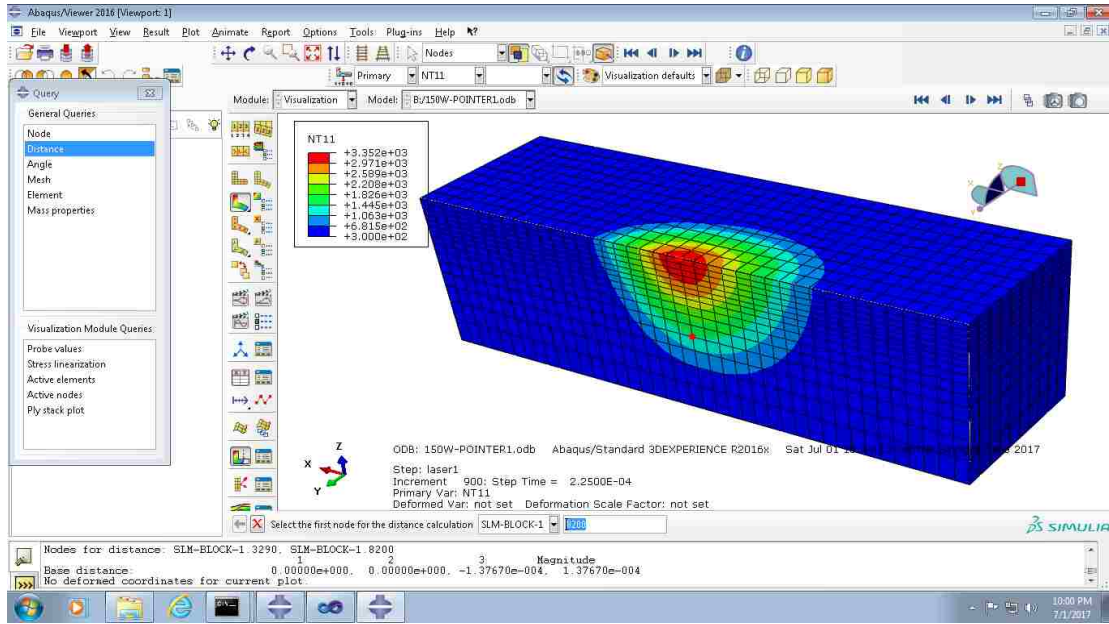


Figure 4.15. Melt Pool Depth for 150W Laser Power (137.6 $\mu$ m)

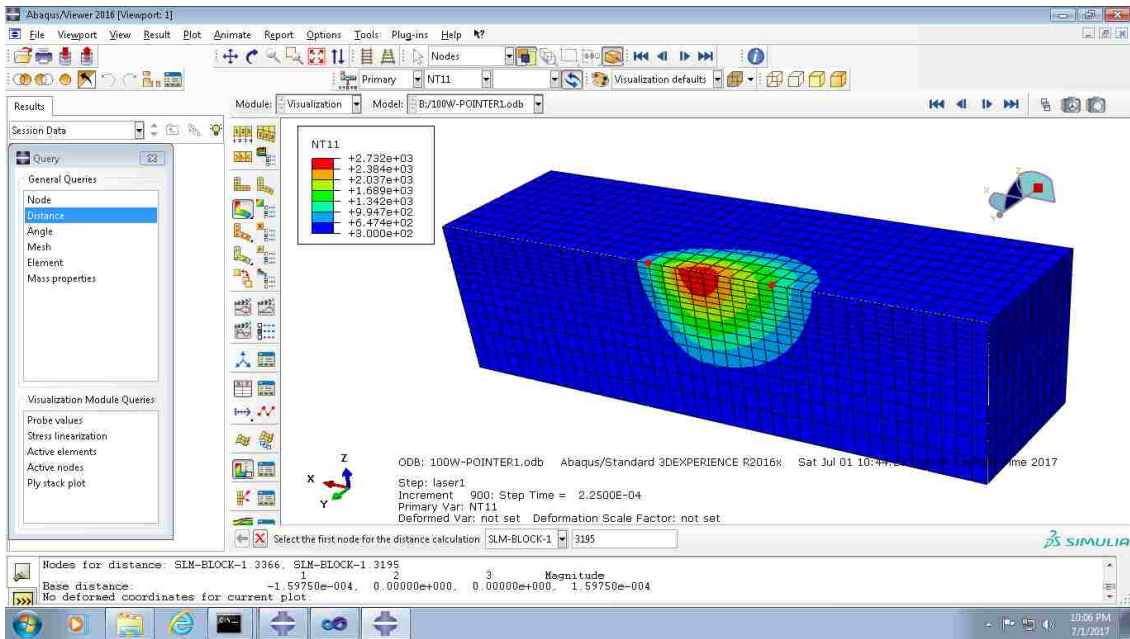


Figure 4.16. Melt Pool Width for 100W Laser Power (159.7 $\mu$ m)

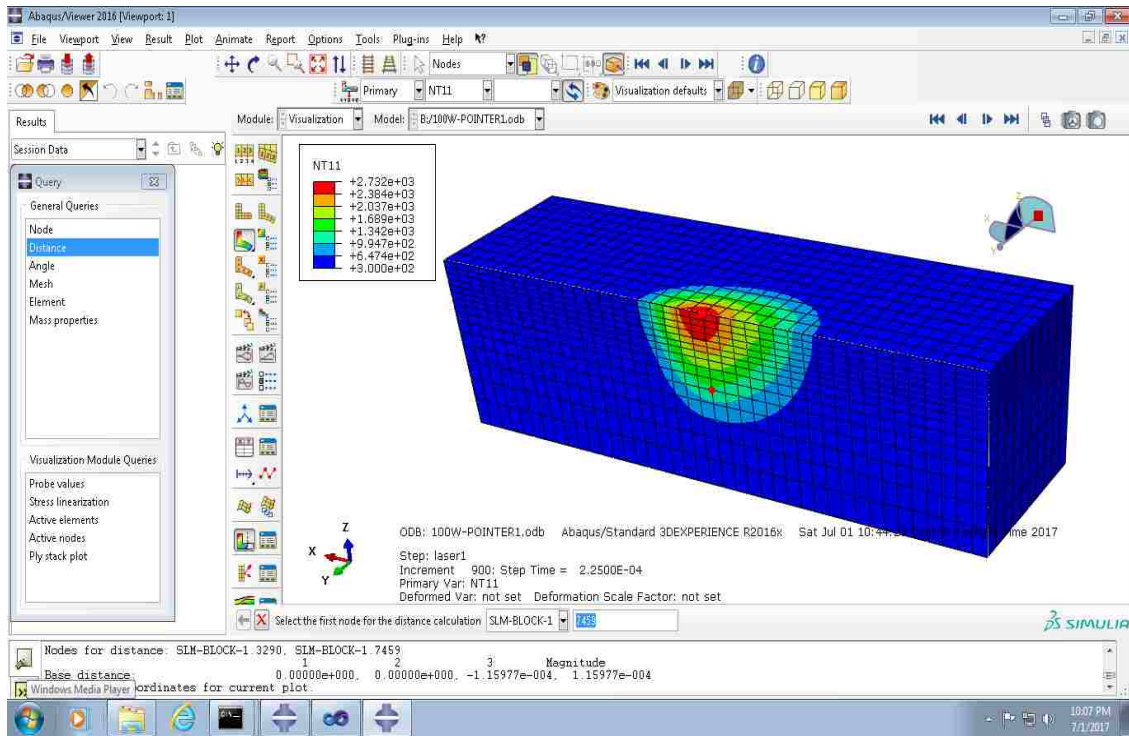


Figure 4.17. Melt Pool Depth for 100W Laser Power (115.9 $\mu$ m)

A comparison between the experimental results and results obtained from ABAQUS output was made and shown in Table 4.5. and 4.6. below.

Table 4.5. Melt Pool Width for a 40 $\mu$ m Point Distance

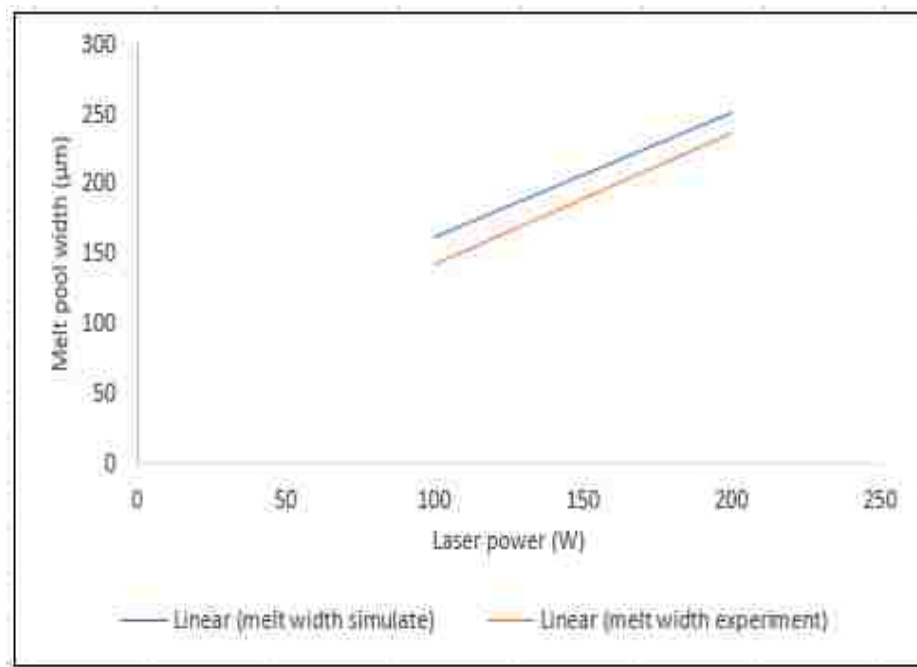
Laser power (W)	Melt width exp. ( $\mu$ m)	Melt width sim. ( $\mu$ m)
100	135	159.7
150	205	213
200	230	248.5



Table 4.6. Melt Pool Depth for a 40 $\mu$ m Point Distance

Laser power (W)	Melt depth exp. ( $\mu$ m)	Melt depth sim. ( $\mu$ m)
100	105	115.9
150	140	137.6
200	220	231.1

A graph of the experimental results and the ABAQUS simulated results as shown in Figures 4.18 and 4.19 below for the melt pool width and melt pool depth respectively also shows a strong correlation.

Figure 4.18. Melt Pool Width: Experimental and Simulated Curves for 40 $\mu$ m Point Distance

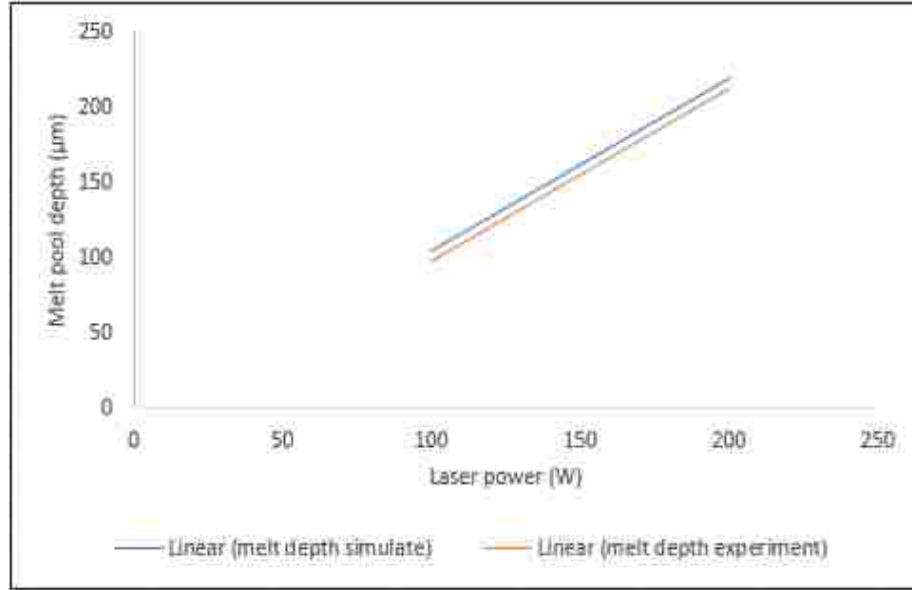


Figure 4.19. Melt Pool Depth: Experimental and Simulated Curves for 40 $\mu$ m Point Distance

Therefore, using the formulation specified in this section, the temperature profile of various laser powers for a 40 $\mu$ m laser point distance can be simulated with good accuracy. As an approximation, the slopes of the melt pool width/depth vs laser power in Figures 4.18 and 4.19 can be assumed linear, and used to predict the melt width and depth for any other laser power input. The slope of the melt pool width curve from Figure 4.18 was:

$$y = (0.95x + 47.5) \mu\text{m} \quad (23)$$

The slope of the melt pool depth from Figure 4.19 was:

$$y1 = (1.15x1 - 17.5) \mu\text{m} \quad (24)$$

where  $y1$  = melt pool depth; and  $x1$  = laser power

Equation (24) above indicates that the laser power is constrained by the value in parenthesis on the RHS (i.e. 17.5). Therefore, with a laser power of 15.217W, the melt pool depth is approximately zero, however the melt pool width will be 61.956 $\mu$ m. This implies that as the laser power decreases, the heat is spread out onto the surface with insufficient heat

penetration to cause melting through the powder bed. In order to obtain sufficient heat penetration through the powder bed especially for low laser powers, the laser pulse duration has to be extended considerably. It therefore suggests that two important parameters that significantly affects the depth of the melt pool are; the laser power and laser pulse duration, all other material properties considered.

Using the ABAQUS model described above, the SLM simulation is repeated with different laser powers and pulse durations to obtain a cooling rate  $\leq 5000\text{C/s}$ , corresponding to the cooling rate with the highest FCC phase fraction from the MatCalc simulation in Figure 3.4. After trying several laser powers; laser power 40W and 50W were selected because they produced cooling rates closest to target cooling rate (i.e.  $\leq 5000\text{C/s}$ ). The procedure for obtaining the cooling rates with a 40W and 50W laser power was the same used for 200W, 150W and 100W. a, b and c for the 50W and 40W laser powers was derived using Equations (18) to (24) above. The values of c and  $M_j$  for the 40W and 50W laser powers is shown in Table 4.7.

Table 4.7. c and  $M_j$  for a 40 $\mu\text{m}$  Point Distance

Laser power (W)	c ( $\mu\text{m}$ )	$M_j$ ( $\mu\text{m}$ )
40	28.50	85.50
50	40.00	95.00

Similarly, the correction factors for heat penetration and heat flux for 50W and 40W laser powers following the same procedure as explained in the previous section for 200W, 150W and 100W are shown in Table 4.8. below.

Table 4.8. Correction Factors for Heat Penetration and Heat Flux

Laser power (W)	Heat penetration factor	Heat flux factor
40	3.0590	0.15087
50	2.4460	0.18859

'a' is simply half of  $M_j$  from Table 4.6 while 'b' is 1/2 of  $\sqrt{M_j^2 - f^2}$ ; and 'f' is (5/7) of  $M_j$  as discussed previously. Results for a and b are shown below in Table 4.9.

Table 4.9. a and b for a 40 $\mu$ m Point Distance

Laser Power (W)	a( $\mu$ m)	b( $\mu$ m)
40	42.750	29.920
50	47.500	33.243

From the results above, it is obvious that the pulse duration for the low laser powers 50W and 40W needs to be extended to ensure a through thickness melting of the powder layer. This involves running several simulations to obtain one whose pulse duration produces an effective through thickness melt. Y. Qin (et.al.) [44]; and Xiaojun T. Yan [45] developed a relationship between thermal penetration depth, time and temperature; and is summarized below.

Y. Qin et. al:

$$\delta(t) = \frac{K_s}{A_s I_0} T_w(t) \quad (25)$$

where

$$T_w(t) = \sqrt{\frac{a_0^2 A_s^2 I_0^2}{8K_s^2} + C_1} \exp\left(-\frac{16\alpha_s t}{a_0^2}\right)$$

and

$$C_1 = -\frac{a_0^2 A_s^2 I_0^2}{8K_s^2}$$

Substituting  $T_w(t)$  and  $C_1$  into Equation (25);  $\delta(t)$  can be reduced to;

$$\delta(t) = \frac{a_0}{\sqrt[2]{2}} \sqrt{1 - \exp\left(-\frac{16\alpha_s t}{a_0^2}\right)}$$

The challenges using these sets of equations is due to fact that it contains several temperature dependent variables (i.e.  $\alpha_s$ ,  $K_s$  and  $A_s$ ) and will also be very difficult to simulate.

Xiaojun T. Yan:

Xiaojun T. provides a more direct equation for relating thermal penetration depth with time as follows;

$$\delta = 3.2125 \sqrt{\alpha t}$$

$$\frac{T(\delta, t) - T_w}{T_i - T_w} = 0.99$$

However, this simplified model does not take material properties or any laser or powder parameters such as porosity and powder size into account; and is therefore not suited for this application. Therefore, modeling a complex process like SLM almost always involves a finite element analysis approach to account for the vast uncertainties that exists in this process.

**4.4.3. Cooling Rate.** To obtain the cooling rates from ABAQUS after the laser pulse stops, two adjacent nodal points are located within the melt pool (the center of the melt pool at the surface of the powder bed was chosen for this study). In ABAQUS, nodes are located in the model by identifying their corresponding node number, which can be obtained by

querying the nodes. Once the node number is obtained, a path from the first node to the second node is created to track changes in temperature along this path at different times during cooling. The next step is creating an XY Data, which is essentially a path-temperature output data from ABAQUS that describes the temperature profile along the specified path at different times during the simulation. Figures 4.20 and 4.21 below highlights important elements of this concept.

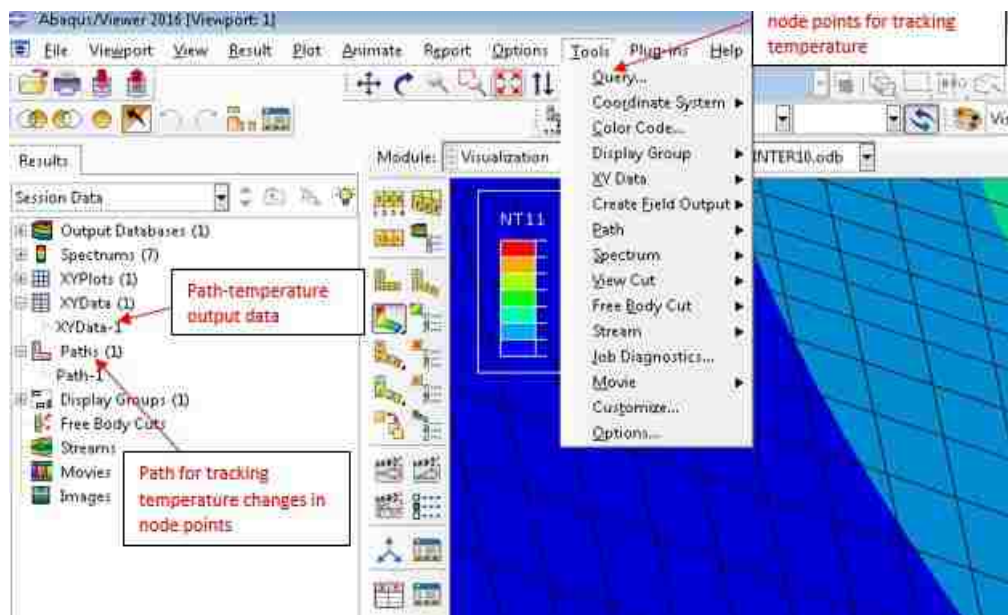


Figure. 4.20. ABAQUS Output Graphic Highlighting Paths, XY-Data and Query

In order to obtain the cooling rates, cooling temperatures obtained from the XY-Data is plotted against time at different time intervals during cooling. Typically, cooling is quite rapid initially and then slows down with time until almost constant or cools down to ambient temperature (300K in this study). The figures below show the graph of cooling rates for various laser powers extracted from ABAQUS output data. The tables for the cooling curve

data points are located in the Appendix at the end of this report. Figures 4.23 to 4.32 show the graphs of the cooling curves for the different laser powers. Figure 4.22 shows a Path-Temperature plot from ABAQUS for a specific time period.

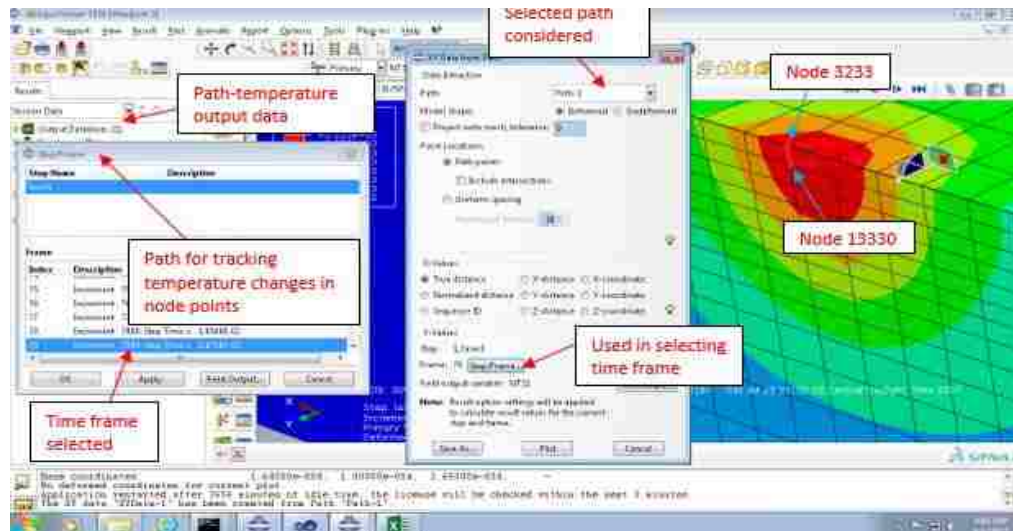


Figure 4.21. ABAQUS Output Graphic Highlighting Time-frame and Selected Path Nodes

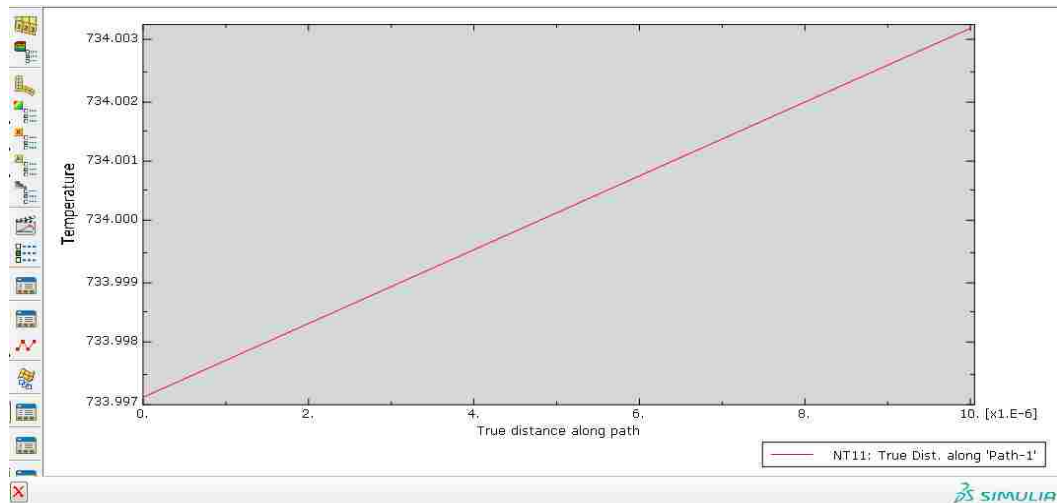


Figure 4.22. Example of an XY-Data Graph from ABAQUS

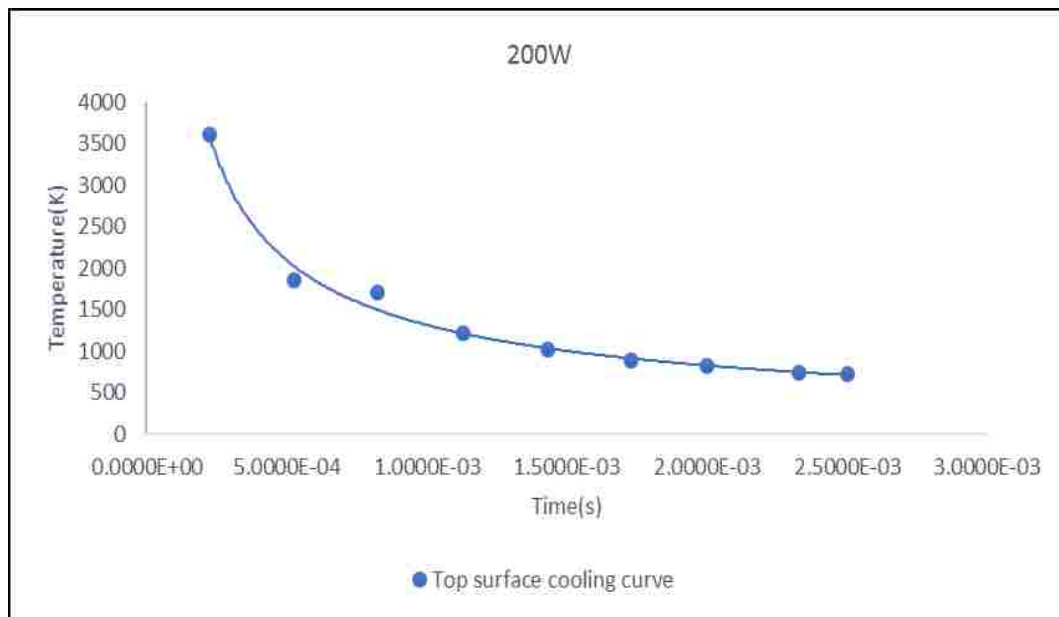


Figure 4.23. Cooling Curve for 200W Laser Power

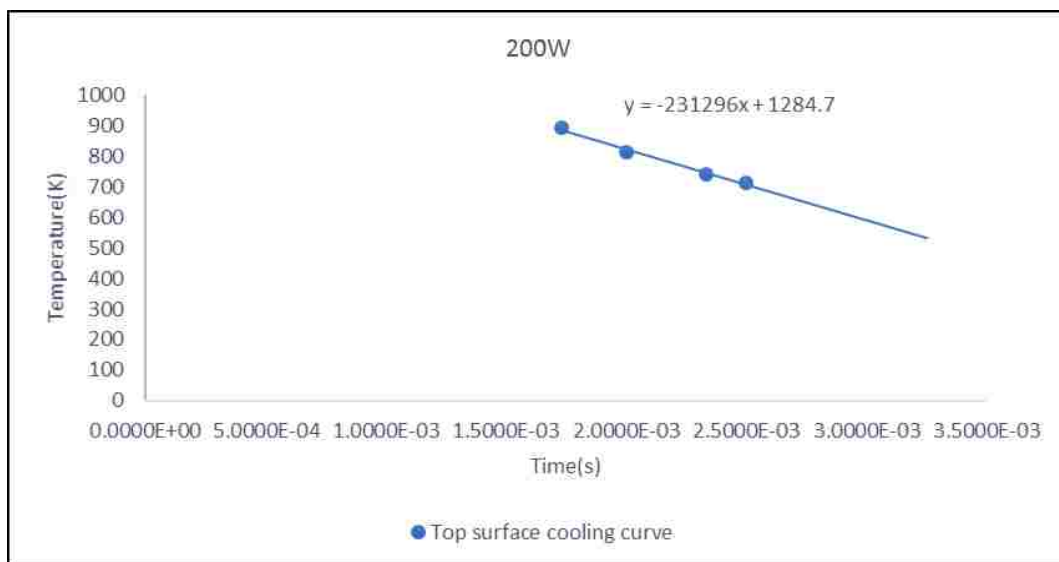


Figure 4.24. Cooling Curve at Constant Slope from Fig. 4.23



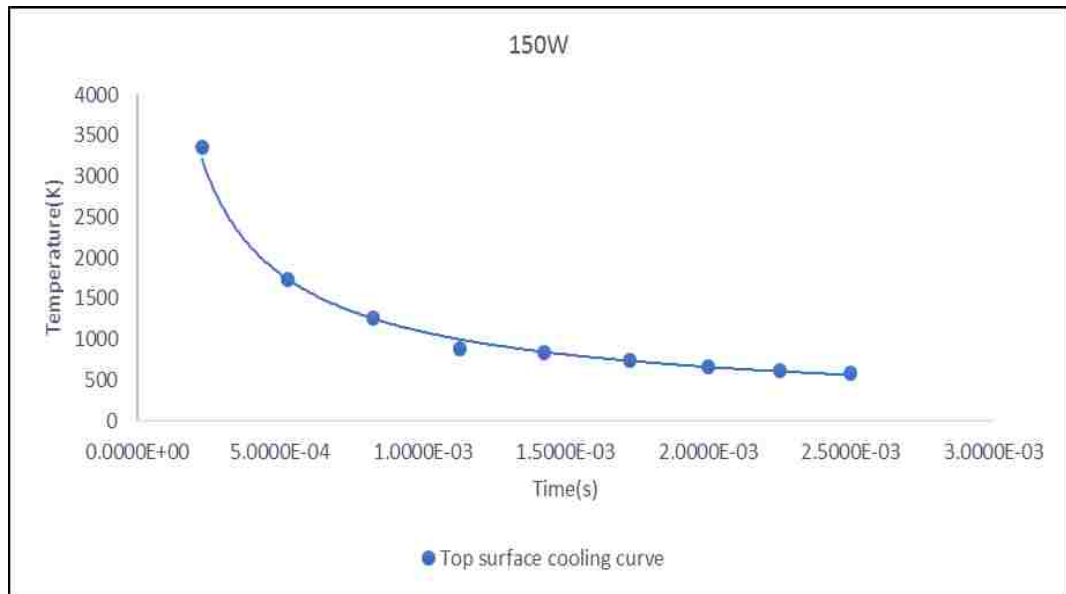


Figure 4.25. Cooling Curve for 150W Laser Power

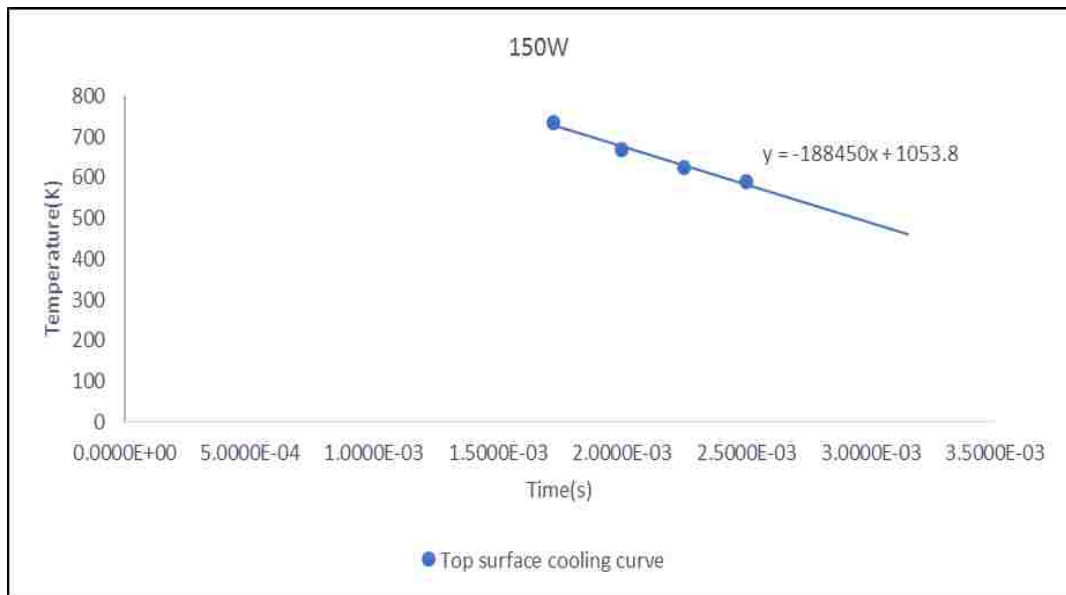


Figure 4.26. Cooling Curve at Constant Slope from Fig. 4.25

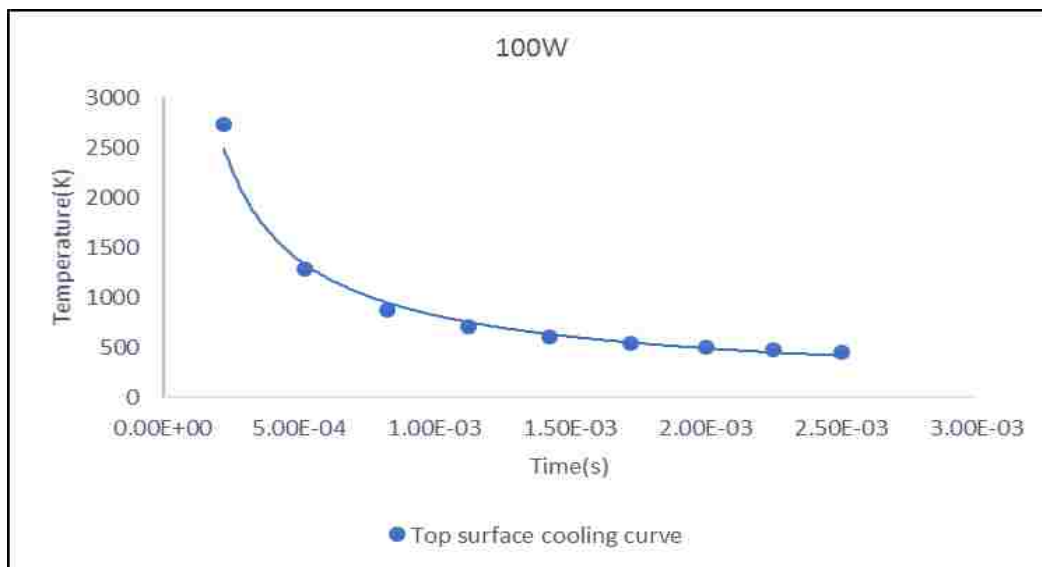


Figure 4.27. Cooling Curve for 100W Laser Power

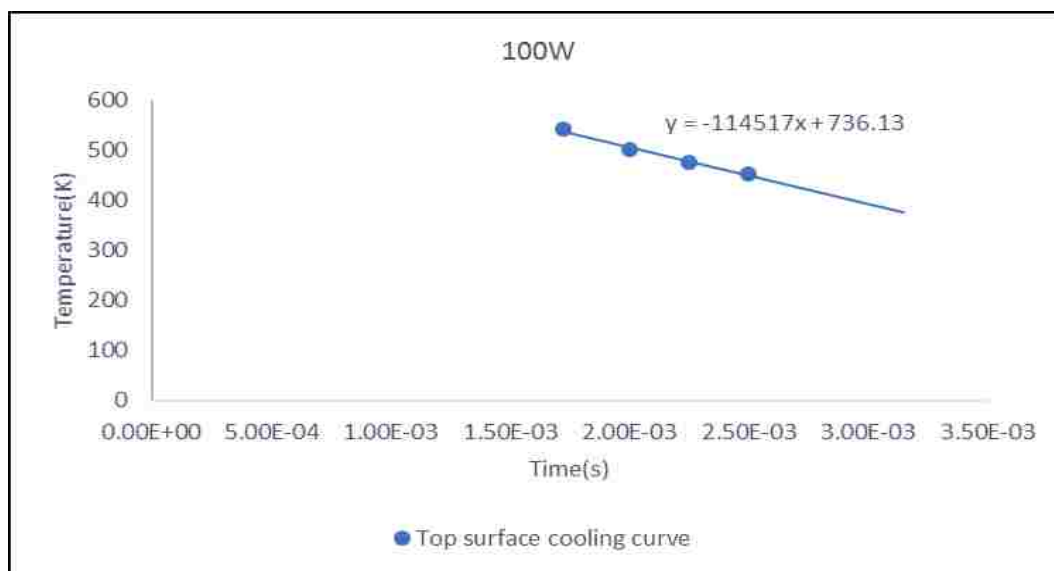


Figure 4.28. Cooling Curve at Constant Slope from Fig. 4.27

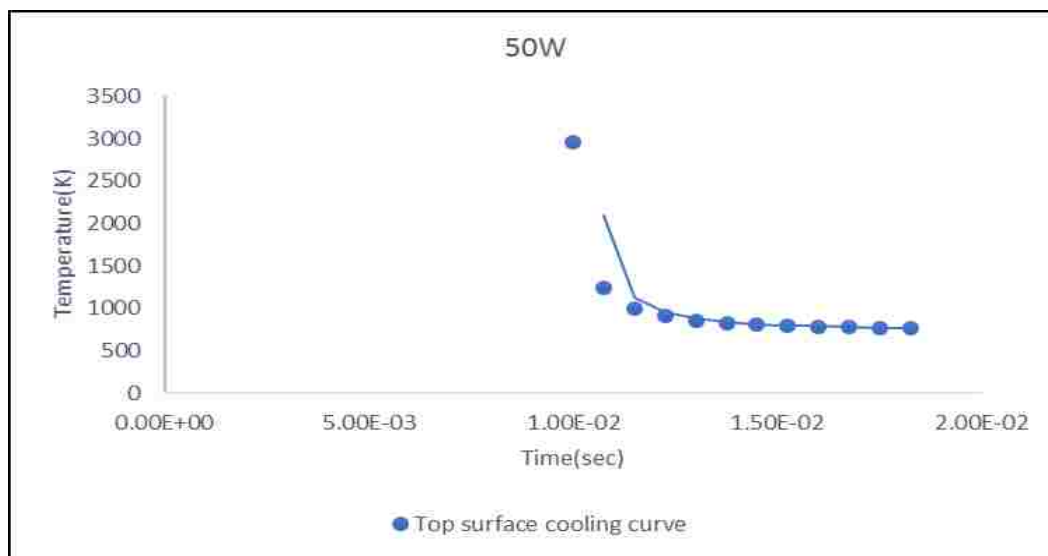


Figure 4.29. Cooling Curve for 50W Laser Power

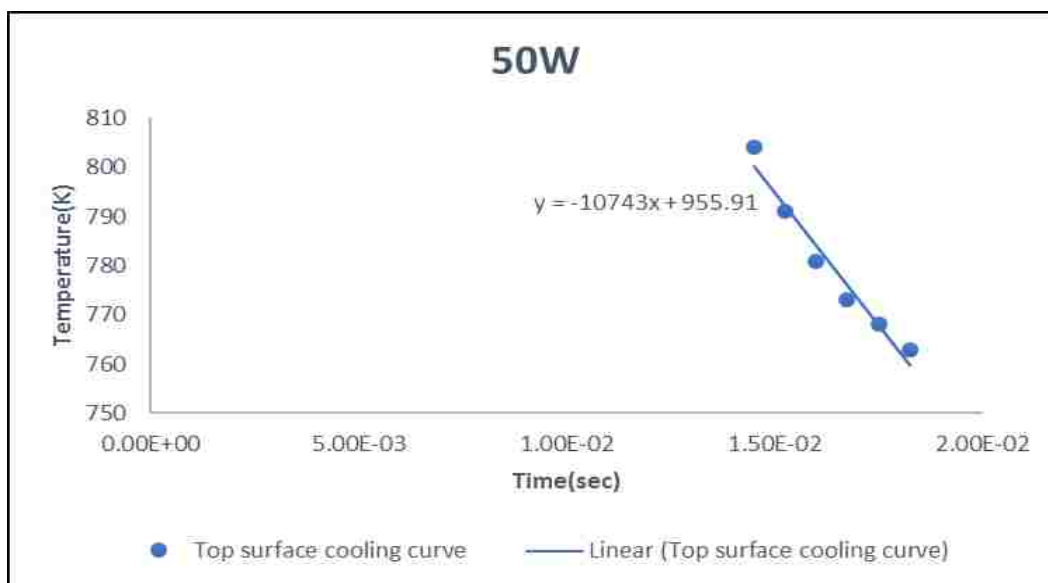


Figure 4.30. Cooling Curve at Constant Slope from Fig. 4.29

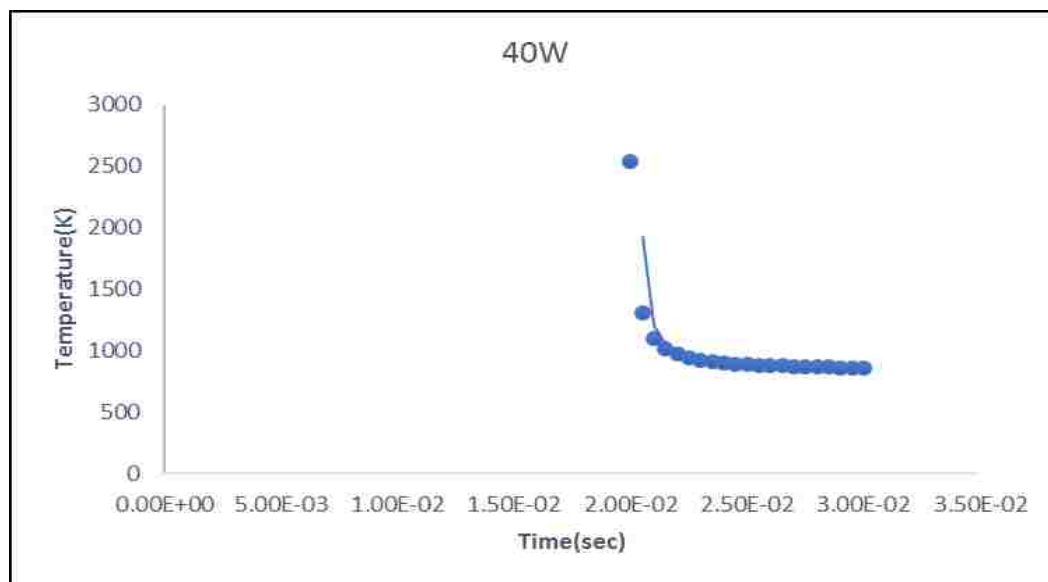


Figure 4.31. Cooling Curve for 40W Laser Power

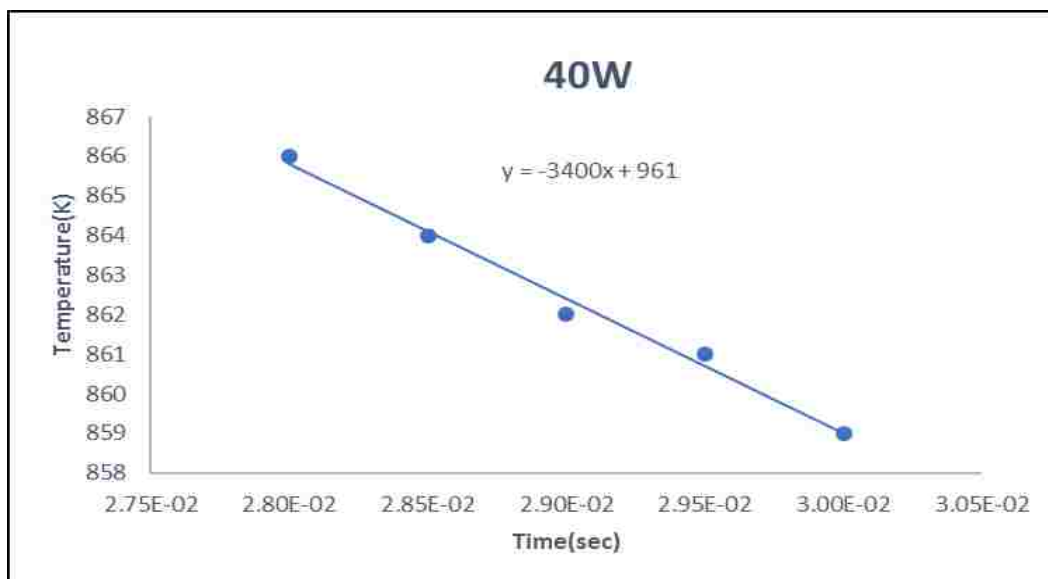


Figure 4.32. Cooling Curve at Constant Slope from Fig. 4.31

## 5. RESULTS AND DISCUSSIONS

The graphs of the cooling rates above show that 40W laser power has a cooling rate (3400K/s) that is closest to the cooling rate from MatCalc for the highest austenite phase fraction (> 90%). This cooling rate also has a straight-line gradient from approximately 866K to ambient which indicates a constant cooling rate within the temperature range where most phase transformation occurs. Decreasing the laser power even further will result to a more fully austenitic alloy. However, this will increase the heating time considerably and may not produce a through thickness melt from top to bottom due to heat losses whose effect is more revealing with very low power input.

The gradient of the cooling curves increases with increasing laser power while the austenite phase fractions increases with decreasing laser power, so that the 200W laser power produces the highest cooling rates (> 230,000K/s). For very rapid cooling rates there's not enough time for the  $\delta \rightarrow \gamma$  transformation from Equation (15); which explains why the highest amount of  $\delta$ (BCC) in the solidified material was greatest with 200W laser power (above 45% BCC). The phase fractions in the 200W laser power can also be described using the Scheil Gulliver model (for rapid cooling) whose principle was described in previous sections of this report. The results for the FCC and BCC phase fractions using Scheil model via ThermoCalc software is shown in Figures 5.1 and 5.2 below. The Scheil result from Figures 5.1 and 5.2 below shows a 63% FCC(Austenite) and 36% BCC(Ferrite).

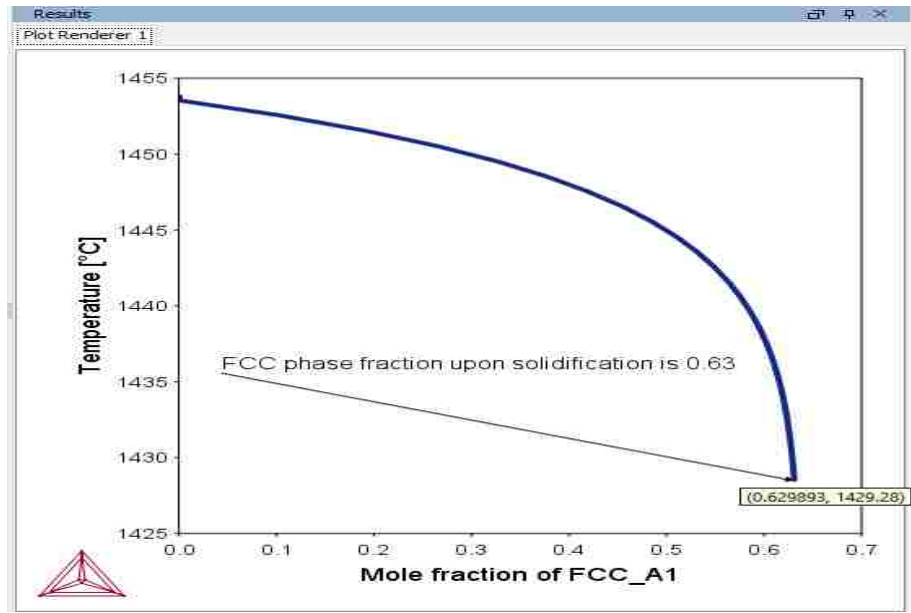


Figure 5.1. Scheil Model Showing FCC-Phase Fraction for Fe (70%), Cr (18%) and Ni (12%) in 304L-SS (ThermoCalc)

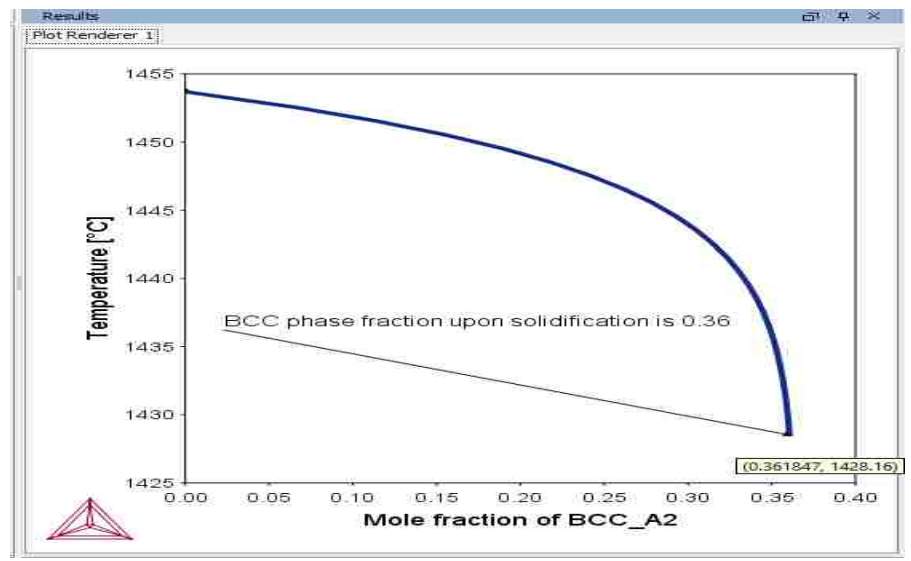


Figure 5.2. Scheil Model Showing BCC-Phase Fraction for Fe (70%), Cr (18%) and Ni (12%) in 304L-SS (ThermoCalc)

Compare the Scheil result from Figures 5.1 and 5.2 with the 55% FCC and 45% BCC obtained from MatCalc for a cooling rate of 100,000K/s. Although their results are not exact, the most important thing to note in both results is that the Scheil model predicts a high percent phase fraction of BCC for rapid cooling rates which was the same when we simulated the phase fractions of FCC and BCC using a diffusional model with a rapid cooling rate of 100,000K/s via MatCalc.

Hence, we can conclude that the laser power affects the cooling rate which also affects the amount of FCC and BCC formed. Rapid cooling rate ( $> 10^5$  K/s) can see a phase fractions of BCC  $> 45\%$ . For moderate cooling rates, the BCC fraction is smaller and at very low cooling rates ( $< 5000$ K/s), the phase fraction of BCC is less than 10% indicating an almost fully Austenitic stainless steel.

## 6. CONCLUSION

This study although focused on 304L Stainless Steel, seeks to draw attention on how the cooling rates could significantly alter the microstructure and phase fractions of metal powders during Selective Laser Melting process. The results show that a traditional 304L-SS which is typically very austenitic may show a marked deviation from its original property to an almost 50-50% austenite (FCC) and ferrite (BCC) composition after consolidating. This change could be very undesirable in very severe corrosive environments since ferrite has a weak corrosion resistance compared to austenite which delivers the high corrosion resistance in 304L Stainless Steels. In addition, some applications where magnetic interference is intolerable could in fact be affected using a consolidated powder with a high BCC fraction since ferrite is magnetic.

Laser power has shown to have a major influence on the cooling rates, with laser powers above 100W producing cooling rates greater than  $10^5\text{C/s}$ . An increased percentage of ferrite was also seen with increasing laser power. Laser powers below 50W shows a dramatic decrease in the cooling rates and BCC fractions such that at 40W laser power an almost austenitic stainless steel (FCC > 90%) is produced. Although a high austenite fraction is desirable for its corrosion resistant properties, there are instances where a controlled amount of ferrite can improve resistance to hot cracking and increase the material strength. Using the strategies adopted in this study can enable the user to control the cooling rates to alter the initial properties of the powder to other desired properties needed. It also serves to study how the microstructure and its phase fractions will evolve and or change after consolidating and how cooling rates does provide a convenient and simple way of controlling these properties during the process.



Another important part of this work was in developing the ABAQUS model subroutine as shown in the Appendix. Investigating the shape of the consolidated melt pool reveals an oval cross-section rather than spherical, so that the Goldak's model proved to be more suitable for modeling the heat flux. To overcome the challenge of obtaining values for  $a$ ,  $b$  and  $c$  in the Goldak's equation, an empirical formula was developed in this study which shows a strong correlation with experimental results. Though, this empirical formula is limited to only 304L Stainless Steels, the procedure outlined in this study can be used to develop similar empirical formulas for other materials.

Results from this study also shows that the cooling rate for any given process is not a constant factor, but evolves with time. Typically, the cooling rates is highest at the initial start of the cooling and then tapers off to an almost constant rate after some time. Rapid cooling ( $10^5$  K/s) associated with high laser powers ( $\geq 100$ W) typically shows a high cooling rate from start of cooling till ambient temperatures. Due to the rapid consolidation associated with high cooling rates, there isn't sufficient time for solid state diffusion, so that the  $\delta \rightarrow \gamma$  (ferrite to austenite) transformation in Equation (15) is suppressed. The result is an increased BCC fraction. On the other hand, a laser power of  $\leq 50$ W starts off with a very high cooling rate and then decreases abruptly to  $< 11,000$  K/s at approximately 800K and remains constant till ambient temperatures. With such low cooling rates at a temperature range where major  $\delta \rightarrow \gamma$  occurs (typically from 950K to 450K); the result is a higher austenite fraction in the consolidated material. This therefore suggests that the phase transformation process could be diffusional, diffusionless or a combination of both occurring at different times in the process depending on the associated cooling rates.

APPENDIX A.  
COOLING RATE TABLES

Table A1. Table for Figure 4.23

Time 45	Temperature
2.2500E-04	3608
5.2500E-04	1848
8.2500E-04	1701
1.1300E-03	1205
1.4300E-03	1016
1.7300E-03	892
2.0000E-03	812
2.3300E-03	742
2.5000E-03	713

Table A2. Table for Figure 4.24

Time 47	Temperature
2.2500E-04	3352
5.2500E-04	1730
8.2500E-04	1262
1.1300E-03	890
1.4250E-03	835
1.7250E-03	735
2.0000E-03	670
2.2500E-03	624
2.5000E-03	589

Table A3. Table for Figure 4.25

Time	Temperature
2.25E-04	2731
5.25E-04	1281
8.25E-04	879
1.13E-03	706
1.43E-03	607
1.73E-03	543
2.00E-03	502
2.25E-03	475
2.50E-03	454

Table A4. Table for Figure 4.26

Time	Temperature
1.00E-02	2954
1.08E-02	1240
1.15E-02	999
1.23E-02	902
1.30E-02	853
1.38E-02	823
1.45E-02	804
1.53E-02	791
1.60E-02	781
1.68E-02	773
1.75E-02	768
1.83E-02	763

Table A5. Table for Figure 4.27

Time	Temperature
2.00E-02	2533
2.05E-02	1305
2.10E-02	1101
2.15E-02	1017
2.20E-02	971
2.25E-02	942
2.30E-02	923
2.35E-02	909
2.40E-02	899
2.45E-02	892
2.50E-02	886
2.55E-02	881
2.60E-02	877
2.65E-02	874
2.70E-02	871
2.75E-02	868
2.80E-02	866
2.85E-02	864
2.90E-02	862
2.95E-02	861
3.00E-02	859

APPENDIX B.  
FORTRAN CODES

FORTRAN Heat Flux Subroutine For 200W Laser Power

**SUBROUTINE** DFLUX(FLUX,SOL,KSTEP,KINC,TIME,NOEL,NPT,COORDS,

**1** JLTYP,TEMP,PRESS,SNAME)

C

**INCLUDE** 'ABA\_PARAM.INC'

C

**DIMENSION** FLUX(2), TIME(2), COORDS(3)

**CHARACTER**\*80 SNAME

q1 = 200

r1 = 115e-6

r2 = 80.49e-6

optd = 1.25\*220e-6

p= 75e-6

y= -0.0001

x0= -0.000155

x1= -0.000195

x2= -0.000235

z1= 0.000275

C

heat=(1.4\*5.8632\*q1\*0.75439)/(optd\*r1\*r2\*3.14159)

**If**(KSTEP.eq.1 .and. time(2).le. p)**THEN**

depth=**exp**(-3\***abs**((COORDS(3)-z1)\*\*2)/(1.23\*optd\*\*2))

shape1=**exp**(-3\*((COORDS(1)+x0)\*\*2/(r1\*\*2)))

shape2=**exp**(-3\*((COORDS(2)+y)\*\*2/(r2\*\*2)))

```

elseif(KSTEP.eq.1 .and. time(2).gt.p .and. time(2).le.2*p)THEN
depth=exp(-3*abs((COORDS(3)-z1)**2)/(1.23*optd**2))
shape1=exp(-3*((COORDS(1)+x1)**2/(r1**2)))
shape2=exp(-3*((COORDS(2)+y)**2/(r2**2)))
elseif(KSTEP.eq.1 .and. time(2).gt.2*p .and. time(2).le.3*p)THEN
depth=exp(-3*abs((COORDS(3)-z1)**2)/(1.23*optd**2))
shape1=exp(-3*((COORDS(1)+x2)**2/(r1**2)))
shape2=exp(-3*((COORDS(2)+y)**2/(r2**2)))
ENDIF
FLUX(1)=heat*shape1*depth*shape2
RETURN
END

```

C

```

SUBROUTINE USDFLD(FIELD,STATEV,PNEWDT,DIRECT,T,CELENT,
1 TIME,DTIME,CMNAME,ORNAME,NFIELD,NSTATV,NOEL,NPT,LAYER,
2 KSPT,KSTEP,KINC,NDI,NSHR,COORD,JMAC,JMATYP,MATLAYO,LACCFLA)

```

C

```

INCLUDE 'ABA_PARAM.INC'

```

C

```

CHARACTER*80 CNAME,ORNAME
CHARACTER*3 FLGRAY(15)
DIMENSION FIELD(NFIELD),STATEV(NSTATV),DIRECT(3,3),
1 T(3,3),TIME(2)
DIMENSION ARRAY(15),JARRAY(15),JMAC(*),JMATYP(*),COORD(*)

```

C Reference current temperature:

CALL

GETVRM('TEMP',ARRAY,JARRAY,FLGRAY,JRCD,JMAC,JMATYP,MATLAYO,

1 LACCFLA)

TEMPERATURE = ARRAY(1)

C Maximum value of temperature up to this point in time:

CALL

GETVRM('SDV',ARRAY,JARRAY,FLGRAY,JRCD,JMAC,JMATYP,MATLAYO,

1 LACCFLA)

TEMPMAX = ARRAY(1)

C Use the maximum temperature as a flag

FLAG = MAX( TEMPERATURE , TEMPMAX )

C Change state when liquidus temperature is reached:

IF (FLAG .gt. 1697) THEN

FIELD(1) = 1

END IF

STATEV(1) = FLAG

C

RETURN

END



## BIBLIOGRAPHY

1. Kruth J.P., Levy, G., Klocke, F., Childs, T.H.C. "Consolidation phenomena in laser and powder-bed layered manufacturing," *CIRP Annals – Manufacturing Technology*, 56(2), 730-759 (2007)
2. Thijs, Lore; Verhaeghe, Frederik; Craeghs, Tom; Humpback, Jan Van; Kruth, Jean-Pierre; "A study of the microstructural evolution during Selective Laser Melting of Ti-6Al-4V," *Acta Materialia* 58(9), 3303–3312 (2010)
3. Gusarov, A.V.; Smurov, I; "Modeling the interaction of laser radiation with powder bed at Selective Laser Melting," *Physics Procedia* 5, 381-394 (2010).
4. J. P. Kruth, B. Vandenbroucke, J. Van Vaerenbergh, and I. Naert, "Digital manufacturing of biocompatible metal frameworks for complex dental prostheses by means of SLS/SLM," in *Proceedings of the VRAP (2005)*, pp. 139-145
5. M. Wehmoller, P. H. Warnke, C. Zilian, and H. Eufinger, "Implant design and production—a new approach by Selective Laser Melting," *Computer Assisted Radiology and Surgery* 1281, 690–695 (2005)
6. I. Yadroitsev, I. Yadroitsava, and I. Smurov; "Laser-Based Micro- and Nano packaging and Assembly V," *Proc. SPIE* 7921, 792101 (2011)
7. M. Wehmoller, P. H. Warnke, C. Zilian, and H. Eufinger, "Implant design and production—a new approach by Selective Laser Melting," *Computer Assisted Radiology and Surgery* 1281, 690–695 (2005)
8. M. A. Garcia, C. Garcia-Pando, and C. Marto, "Conformal Cooling in Molds with Special Geometry," (CRC Press, p. 409–412. (2012)
9. M. Santorinaios, W. Brooks, C. J. Sutcliffe, and R. A. W. Mines, "Crush behaviour of open cellular lattice structures manufactured using Selective Laser Melting," in *High Performance Structures and Materials III*, C.A. Brebbia, ed. (WIT Press, 2006)
10. J.C. Lippold and W.F. Savage, "Solidification of Austenitic Stainless-Steel Weldments. 1--A.--Proposed Mechanism," *Welding Journal* 58(12), 362 (1979).
11. G. L. Leone and H. W. Kerr, "The ferrite to austenite transformation in stainless steels," *Welding Journal* 61(1), 13S-21S (1982).
12. S. David, J. Vitek, R. Reed, T. Hebble, Effect of rapid solidification on stainless steel weld metal microstructures and its implications on the Schaeffler diagram, Oak Ridge National Lab., TN (USA)1987.
13. Angelo Fernando Padilha, Caio Fazzioli Tavares, Marcelo Aquino Martorano; "Delta Ferrite Formation in Austenitic Stainless-Steel Castings," *Materials Science Forum Vols.* 730-732, pp 733-738 (2013)

14. Kamran Saeidi; "Stainless steels fabricated by laser melting," Department of Materials and Environmental Chemistry, Arrhenius Laboratory, Stockholm University, SE-106 91 Stockholm, Sweden; Doctoral Thesis (2016)
15. Kujanpaa V. P, David S. A., and White C. L. "Formation of hot cracks in austenitic stainless-steel welds — solidification cracking," *Welding Journal* 65(8): 203-sto 212-s, (1986)
16. Ogawa, T. and Tsunetomi E.; "Hot cracking susceptibility of austenitic stainless-steel welds," *Proceedings of the 10th Golden Gate Metals and Welding Conference*, San Francisco, Calif. (1979)
17. Backman A., and Lundquist B.; "Properties of a fully austenitic stainless-steel weld metal for severe corrosion environment," *Welding Journal* 56(11), 23-s to 28-s, (1977)
18. W. T. Delong; "Ferrite in Austenitic Stainless-Steel Weld Metal," *Weld. J.*, vol. 53, no. 7, pp. 273s-86s (1974)
19. R. Castro and J. J. de Cadenett; "Welding Metallurgy of Stainless and Heat Resisting Steels," Cambridge University Press, London, 1974.
20. "Ferrite Content in Austenitic Stainless Steels," <https://www.rolledalloys.com/technical-resources/blog/ferrite-content-in-austenitic-stainless-steels>, 8/19/2017
21. Taha Mustahsan. "Advantages and disadvantages of different casting processes" Roll #14, Reg #-UET-IEFR-MECH-FD-08, PP1-8 (2008)
22. T. Trosch, J. Strobner, R. Volkl and U. Glatzel "Microstructure and mechanical properties of selective laser melted Inconel 718 compared to forging and casting." Vol 164, p428-431 (2016)
23. H.K.D.H. Bhadeshia, "Additive manufacturing of metals for aerospace applications/advanced metallic alloys for the fossil fuel industries," *Materials Science and Technology* issue 7 vol. 32, p 615-616 (2016)
24. S.S. Badu & R. Goodridge "Additive manufacturing" vol. 31 issue 8 *Material Science Technology Journal* pp 881-883 (2016)
25. William E. Frazier; "Metal Additive Manufacturing: A Review," *ASM International Vol. 23(6), Journal of Materials Engineering and Performance*; pp 1917-1928 (2014)
26. Zhou Wei. Presentation at general engineering and safety standards committee (GESSC) standards exchange, Singapore (2013)
27. T.S. Srivatsan, K. Manigandan, T.S. Sudarshan. "Additive manufacturing of materials, viable techniques, metals, advances, advantages and applications," Taylor and Francis group LLC, pp25 (2016)

28. L. Thijs, F. Verhaeghe, T Craeghs, Jan Van Humbeeck, Jean-Pierre Kruth; "A study of the microstructural evolution during Selective Laser Melting of Ti-6Al-4V," vol. 58, issue 9, pp 3303-3312 (2010)
29. E. Yasa, J.P. Kruth "Microstructural Investigation of Selective Laser Melting 316L stainless steel parts exposed to laser re-melting." *Procedia Engineering* 19, pp389-395 (2011)
30. Wei-Chin Huang, Chuan-Sheng Chuang, Ching-Chin Lin, Chih-hsren Wu, De-Yau Lin, Sung-Ho Liu, Wen-Peng Tseng, Ji-Bin Horng. "Microstructure controllable laser additive manufacturing process for metal products," Vol. 56, *Physics Procedia*, pp 56-63 (2014).
31. S. Dadbakhsh and Liang Hao. "Effect of layer thickness in Selecting laser melting on microstructure of Al/5 wt % Fe<sub>2</sub>O<sub>3</sub> powder consolidated parts," *The scientific world journal* vol. 2014, Article ID: 106129, (2014)
32. "Ferrite Content in Austenitic Stainless Steels," <https://www.rolledalloys.com/technical-resources/blog/ferrite-content-in-austenitic-stainless-steels>, 8/19/2017
33. K. Jackson, "Kinetic Processes: Crystal growth, diffusion and phase transitions in materials", pp 136-137 2nd edition, Wiley-VCH (2004)
34. David A. Porter, Kenneth E. Easterling, and Mohamed Y. Sherif, in *Phase Transformations Metals and Alloys*, CRC Press (2009)
35. P. Alope and S. Divinski, "Handbook of solid state diffusion: diffusion fundamentals and techniques", vol. 1, chapter 8, pp391- 395 (2017)
36. F.D. Fischer, J. Svoboda, H. Petryk; "Thermodynamic extremal principles for irreversible processes in materials science", *Acta Materialia*, vol. 67, p 1-20 (2014)
37. Takalo T, Suutala N, Moisiö T, "Austenitic solidification mode in austenitic stainless-steel welds", *Metall Trans A* 10A:1173–1181 (1979)
38. Suutala N; "Effect of solidification conditions on the solidification mode in austenitic stainless steels", *Metal Trans A* 14A, 191–197 (1983)
39. Huang FX, Wang XH, Wang WJ, "Microstructures of austenitic stainless steel produced by twin-roll strip caster", *J Iron Steel Res Int.* 19:57–61 (2012)
40. Congfeng Wu, Shilei Li, Changhua Zhang, Xitao Wang; "Microstructural evolution in 316LN austenitic stainless steel during solidification process under different cooling rates", *Journal of material science*, Volume 51, Issue 5, pp 2529–2539, (2016)
41. Hammar O., Svensson U.; "Influence of steel composition on segregation and microstructure during solidification of austenitic stainless steels", *Solidification and Casting of Metals Proceedings*, The Metals Society, London (1979).

42. John Goldak, Aditya Chakravarti, Malcolm Bibby; "A new finite element model for welding heat sources," *Metallurgical Transactions B*, 15(2), 299-305 (1984).
43. Bonifaz, E.A., "Finite element analysis of heat flow in single-pass arc welds," *Welding Res. Supplement*, pp:121-125, 2000
44. Y. Qin, B. Wang, X.W. Ni, Z.H. Shen, J. Lu, "Axisymmetric analytical solution for pulsed laser melting of metals," *Computational Material Science* 54, 1-6 (2012)
45. Xiaojun Terry Yan, "On the penetration depth in fourier heat conduction," in *Proceedings of 8th AIAA/ASME Joint Thermophysics and Heat Transfer Conference*, (AIAA, 2002,) pp. 1-6; 24-26
46. Aniruddha Ghosh, Sergej Hloch, Somnath Chattopadhyaya, "Critical analysis of moving heat source shape for arc welding process of high deposition rate," *Tehnički Vjesnik* 21, 1(2014), 95-98
47. Huang, L.J. Yang, X.Z. Du, Y.P. Yang, "Finite element analysis of thermal behavior of metal powder during Selective Laser Melting," *International Journal of Thermal Sciences* 148 (2015)
48. H.S. Carslaw and J.C. Jaeger; *Conduction of Heat in Solids* (Clarendon Press, 1959).
49. Sakae, Yagi; Daizo, Kunii; Noriaki Wakao; "Studies on effective thermal conductivity in packed bed," *Alche Journal* 3(3) 373-381 (1957)
50. P. Zehner and E. U. Schlünder, "Wärmeleitfähigkeit von Schüttungen bei mäßigen Temperaturen," *Chemie Ingenieur Technik*, 42(14), 933-941 (1970)
51. Swaren Bedarkar, Nurni Neelakantan Viswanathan; Nidambur Bharatha, Ballal "Measurement of thermal conductivity along the radial direction in a vertical cylindrical packed bed," *Journal of Powder Technology*, (2015)
52. E.I. Marchenkov; V.I. Aleinikova; "Thermal conductivity of Argon and Argon-Neon mixtures at high temperature," Vol. 33, Issue 5, pp 1318-1324 (1977)
53. C.Y. Ho; T.K. Chu; "Thermal conductivity and electrical resistivity of eight selected AISI stainless steels," prepared for American Iron and steel institute; CINDAS report 45, Table II, pp. 15 (1977)
54. Garofalo, F., Malenock, P. R., and Smith, G. V., "The Influence of Temperature on the Elastic Constants of Some Commercial Steels," *ASTM Spec, Tech, Pub. No. 129*, pp. 10 (1952)

## VITA

Eberechukwu Anthony Okoro was born in Port Harcourt, Nigeria. He obtained his Associate degree and Undergraduate degree both in Mechanical Engineering from Federal Polytechnic Nekede and Akanu Ibiam Federal Polytechnic, Nigeria, in 2002 and 2007 respectively. He also received a Graduate certificate in Engineering Mechanics from Missouri University of Science and Technology in 2015 and a Master's degree in Mechanical Engineering from Missouri University of Science and Technology in May 2018.